Biomaterials 146 (2017) 115–135

Contents lists available at ScienceDirect

Biomaterials

journal homepage: www.elsevier.com/locate/biomaterials

Review

AIEgens for biological process monitoring and disease theranostics

Xinggui Gu [a, b, d, 1], Ryan T.K. Kwok [a, b, 1], Jacky W.Y. Lam [a, b], Ben Zhong Tang [a, b, c, *]

[a] Hong Kong Branch of Chinese National Engineering Research Centre for Tissue Restoration and Reconstruction, Department of Chemistry, Institute for Advanced Study, Institute of Molecular Functional Materials, State Key Laboratory of Molecular Neuroscience, Division of Life Science, The Hong Kong University of Science and Technology (HKUST), Clear Water Bay, Kowloon, Hong Kong

[b] Guangdong Provincial Key Laboratory of Brain Science, Disease and Drug Development, HKUST-Shenzhen Research Institute, No. 9 Yuexing First RD, South Area, Hi-tech Park, Nanshan, Shenzhen, 518057, China

[c] Guangdong Innovative Research Team, SCUT-HKUST Joint Research Laboratory, State Key Laboratory of Luminescent Materials and Devices, South China University of Technology, Guangzhou, 510640, China

[d] Beijing Advanced Innovation Center for Soft Matter Science and Engineering (BAICAS), Beijing University of Chemical Technology, Beijing, 100029, China

ARTICLE INFO

Article history:
Received 29 June 2017
Received in revised form
29 August 2017
Accepted 2 September 2017
Available online 4 September 2017

Keywords:
Biological process
Diagnosis
Theranostics
Aggregation-induced emission
AIE

ABSTRACT

Biological processes are of great significance for the normal physiological functions of living organisms and closely related to the health. Monitoring of biological processes and diagnosis of diseases based on fluorescent techniques would provide comprehensive insight into mechanism of life and pathogenesis of diseases, precisely guiding therapeutic effect in theranostics. It largely relied on fluorophores with the properties of excellent photostability, large Stokes shift, high signal-to-noise ratio and free of aggregation-caused quenching (ACQ) effect. Luminogens with aggregation-induced emission characteristic (AIEgens) could serve as superior agents for biological process monitoring and disease theranostics. Herein, we review the recent results in the aspects of monitoring biological processes such as autophagy, mitophagy, mitochondrion-related dynamics, cell mitotic, long-term cellular tracing and apoptosis as well as the diagnosis of related diseases based on AIEgens in real time. As part of AIEgens and AIEgen-based nanoparticles with the functionalities of drugs, photosensitizers and adjuvants accompanied with imaging, they exhibit huge potential in theranostic systems for image-guided chemotherapy, photodynamic therapy, radiotherapy and so on. Collectively, these examples show the potentials of AIEgens for understanding disease pathogenesis, for drug development and evaluation, and for clinical disease diagnosis and therapy. Future research efforts focused on developing long-wavelength excitable and phosphorescence-emissive AIEgens with improved depth-penetration and minimized background interference for fluorescence and photoacoustic imaging, will extend the potential applications of AIEgens in *in vivo*.

1. Introduction

Biological processes are recognized as a series of biochemical reactions, events and molecular functions that occur in living organisms and are vital for a living organism to live [1]. These processes are specifically pertinent to the function of living cells, tissues and organisms. At molecular level, the actions of biomacromolecules are closely associated with the life. For example, protein-associated activities such as enzyme-catalyzed biochemical reactions in metabolism allow organisms to grow and reproduce, to maintain their structures and respond to environment [2]. The replication and transcription of nucleic acids are critical for the storage and use of genetic information as well as protein biosynthesis [3]. While in cells, subcellular organelles involve in many cellular processes and exert their specific effects on maintaining the normal physiological functions, such as lysosome-mediated autophagy for degradation of damaged substrates inside cells [4], nucleus-related gene expression, post-transcriptional modification and cell division [5], Golgi apparatus-assisted sorting, packaging, processing and modification of proteins [6], and mitochondrion-

* Corresponding author. Hong Kong Branch of Chinese National Engineering Research Centre for Tissue Restoration and Reconstruction, Department of Chemistry, Institute for Advanced Study, Institute of Molecular Functional Materials, State Key Laboratory of Molecular Neuroscience, Division of Life Science, The Hong Kong University of Science and Technology (HKUST), Clear Water Bay, Kowloon, Hong Kong.

E-mail address: tangbenz@ust.hk (B.Z. Tang).

[1] X. Gu and R. T. K. Kwok contributed equally in this review.

http://dx.doi.org/10.1016/j.biomaterials.2017.09.004
0142-9612/

associated energy generation [7]. Cell events such as differentiation and apoptosis also play critical roles in cellular renewal and maintain balance of the whole organisms [8,9]. Consequently, biological processes are of great significance for the normal physiological functions of living organisms and closely related to the health.

On the other hand, the deregulation and abnormality of biological processes could lead to severe diseases such as cancer, Alzheimer's disease and diabetes mellitus. Cancer is a group of diseases involving abnormal cell growth with the potential to invade or spread to other parts of the body [10]. Alzheimer's disease seriously threatens the brain due to neurodegenerative disorders, which are mainly caused by the large-scale aggregation of β-amyloid protein to form plaques [11]. Diabetes mellitus is a group of metabolic diseases caused by the lack of insulin which is a hormone in bloodstream to convert the blood glucose to glycogen [12]. Supposing that disease-related biological processes, such as enzyme-catalyzed reactions, protein fibrosis, abnormal mitochondria dynamics, pathological apoptosis, cancer proliferation, invasion, and metastasis, could be monitored on-site and in-time, it would benefit the deep insight into pathogenesis of diseases and precisely guide therapeutic effect in theranostics. Therefore, development of techniques that enable real-time monitoring and long-term tracing biological processes with high resolution and sensitivity is of critical importance in both fundamental biological science and practical clinical applications.

To date, many techniques have been utilized in monitoring and visualizing biological processes. Electron microscopes such as scanning electron microscope (SEM) [13] and transmission electron microscope (TEM) [14] can provide very high image resolution but they are complicated in sample preparation and operation. Besides, the sample must be fixed on the substrate and investigated under vacuum, thus study on cell dynamic is hardly realized. Positron emission tomography (PET) [15] and computed tomography (CT) [16] are imaging techniques that are used to observe metabolic processes in the body, however, they have drawbacks of low resolution, radiation exposure risk, contrast medium harmful for health and complex equipment with high cost. Magnetic resonance imaging (MRI) [17] exhibits high resolution and sensitivity as well as label free, however the cost is very high and the throughput is rather low. The operation cost of ultrasound [18] is low and easy to access. Unfortunately, it bears very low resolution and signal-to-noise ratio. Because of these shortages, all of them are difficult to be used to monitor the biological processes *in situ*. Recently, emerging fluorescent techniques as new approaches have been widely used in biomedical domain especially in observation of cellular and molecular events [19–22], as they possess the advantages of high resolution, sensitivity and contrast, simple and fast operation, and real-time fashion. The Nobel Prizes in 2008 and 2014 were presented to the scientists who worked in the field of fluorescent materials and techniques.

Thanks to the enthusiastic effort by researchers, various types of fluorescent probes and techniques were developed for biological imaging. Fluorescent proteins (FPs) [23] show high selectivity and biocompatibility but they suffer from inevitable decomposition by enzymes, high cost and easy photobleaching. Quantum dots (Q dots) [24] enjoy high emission efficiency and facile biomodification, but their variety is limited and cytotoxicity is still a major concern. In comparison, organic fluorophores are relatively less toxic than the heavy metal-containing Q dots [25]. And their emission can be readily tuned by molecular engineering, however, conventional organic fluorophores encounter aggregation-caused quenching (ACQ) effect due to the π-π stacking [26]. As shown in Fig. 1A, fluorescein (**1**), in dilute water solution, displays strong

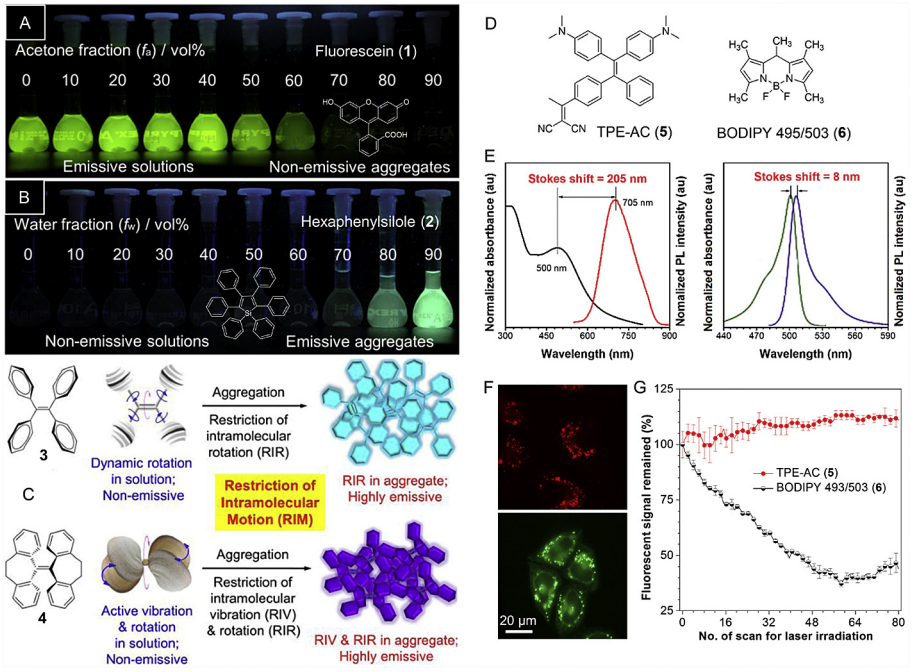

Fig. 1. (A and B) ACQ and AIE phenomena: fluorescent images of solutions and aggregate suspensions of (A) fluorescein (**1**, 15 μM) in water/acetone mixtures with different fractions of acetone (f_a), and (B) hexaphenylsilole (**2**, 10 μM) in THF/water mixtures with different fractions of water (f_w). (C) Restriction of intramolecular motion (RIM) mechanism for AIE: propeller-shaped tetraphenylethene (TPE, **3**) is non-emissive when dissolved but becomes emissive after aggregated, due to the restriction of the intramolecular rotations of its phenyl rotors. Shell-like annulenylidene (**4**) shows AIE activity, due to the restriction of the intramolecular vibration of its bendable vibrators. Images are taken from Ref. [26] with permission. (D) Structures of AIE-active TPE-AC (**5**) and ACQ-featured BODIPY 495/503 (**6**) for lipid droplet imaging. (E) Comparison on the Stokes shift of **5** and **6**. (F) Comparison on the background emission and specificity of **5** and **6** in lipid droplet imaging. (G) Comparison on the photostability of **5** and **6** under laser irradiation. Images are taken from Ref. [29] with permission.

green emission but its emission nearly is quenched when poor solvent acetone is added to induce aggregation of **1**. Due to the detrimental quenching of their light emission by ACQ effect, the recommended concentration used for most conventional fluorophores is very low, which results in low resistance to photobleaching, low signal-to-noise ratio and poor photosensitivity. Therefore, the ACQ effect seriously restricts the applications of fluorophores in various areas.

A new class of luminescent materials with aggregation-induced emission (AIE) characteristic has been emerged since 2001 [27]. Fig. 1B shows the typical AIE-active hexaphenylsilole (**2**) for example [26], unlike the fluorescein, **2** is almost nonemissive in dilute solution but become highly emissive in the aggregated state. The mechanism of AIE is briefly illustrated in Fig. 1C. In solution, dynamic rotation and active vibration in AIE luminogens (AIEgens) such as **3** and **4** largely consume the excited state energy resulting in nonradiative relaxation. Upon aggregation, these kinds of intramolecular motions are restricted to impede the nonradiative relaxation, activating the radiative delay to emit strongly. The AIE mechanism is unified as the restriction of intramolecular motions (RIM) [28], which could guide the design of AIEgens of high desire. Comparing with traditional ACQ fluorophores, AIEgens inherently enjoy the merits of higher brightness, better photostability, turn-on fashion, and larger Stokes shift (taking AIE-active TPE-AC (**5**) and ACQ-featured BODIPY 495/503 (**6**) as the examples illustrated in Fig. 1D–G) [29], encouraging researchers to develop various AIEgens as fluorescent visualizers for biological imaging and monitoring of biological processes.

Traditional theranostic systems are based on the combination of different molecules such as imaging-functional probes and therapeutic agents [30]. These molecules are brought together by molecular engineering and nanotechnology. Recent studies have demonstrated that AIEgens not only act as probes for diagnostic imaging of disease-related substrates or processes in the manner of bright emission, high resistance to photobleaching, large contrast, long-term and real-time monitoring, but also perform well as drugs or photosensitizers for chemo- and photodynamic therapy (PDT) of diseases [31]. Furthermore, AIEgens with the integration of imaging and therapy will provide us deeper insights into the pathogenesis and facilitate the drug development. Thus, multifunctional systems based on AIEgens allow them unique and promising potential in theranostic bearing with the simple and fast fashion.

Since AIEgens with excellent properties have been developed rapidly in various areas such as OLEDs, sensors, energy, environment, anti-counterfeiting, national safety, bioimaging and therapy, much work has been reviewed in recent years [26,28,32–44]. In this review, we use a new angle to summarize the latest results in the aspects of monitoring biological processes such as autophagy, mitochondrion-related dynamics, cell mitotic, stem-cell differentiation and apoptosis as well as the theranostics of diseases, in order to introduce AIEgens to the researchers who are working in area of biomedical science. Due to the limitation of space, we mainly review the AIE research work in recent three years.

2. Biological processes monitoring

Biological processes involve lots of events associating with the dynamic processes of subcellular organelles, enzymes, and so on [1]. Thus, monitoring of the behaviors of organelles and enzymes has been identified as a direct and necessary approach for well understanding of the related biological processes. Development of suitable fluorescent probes for monitoring the dynamics of organelles and enzymes will facilitate the fluorescent visualization of biological processes in high resolution, real-time and long-term, which highly desires the fluorescent probes possess high organelle-specificity, high resistance to photobleaching, intense brightness and large signal-to-noise ratio. Therefore, AIEgens modified with various targeting groups could serve as superior imaging agents for monitoring of the dynamics of various biological process-related organelles and enzymes. And a variety of AIEgens have been developed for monitoring multifarious biological processes, such as autophagy, mitophagy, mitochondrial dynamics, mitosis, stem-cell differentiation, and apoptosis, and representative examples have been reviewed as follow.

Autophagy is a regulated biological process that degrades unnecessary cells and recycles cellular components [45]. Understanding the mechanism of autophagy has been spotlighted in scientific research recently. To acknowledge the outstanding contribution and achievement in the research of autophagy, three scientists had awarded the Nobel Prize in medicine in 2016. It has been found that autophagy is closely associated with many diseases such as cancerous and neurodegenerative diseases [46]. Investigation and monitoring of autophagy is thus of great importance for revealing the mechanism of autophagy and guiding the development of drugs for the diseases.

Typically, autophagy is initialized by the formation of a phagophore, a double membrane enclosing and isolating in the cytoplasmic components. Then, autophagosome will form and deliver the damaged cytoplasmic components to the lysosomes. The subsequent fusion of an autophagosome and lysosomes leads to the formation of autolysosome, where the encapsulated materials will then be degraded by lysosomal hydrolases. After the digestion, lysosomes reform and fuse with next autophagosome [47]. Throughout the whole process, lysosome is the determining subcellular organelle and plays a critical role, thus visualizing and tracking lysosomal activities could provide deeper insight into the autophagy and mechanistic understanding of drug actions. With this regard, various lysosome-specific probes have been designed for studying lysosome-involved cellular activities. LysoTracker Red DND-99 (LTR) is one of the most representative commercial lysosome fluorescent probes [48]. Due to the ACQ effect, it is recommended to be used at very low concentration. As a single molecular species, however, the LTR molecules are easily photobleached. Furthermore, LTR suffers from small Stokes shift and self-absorption, leading to severe limitation of the excitation and emission ranges for high-resolution imaging. Therefore, lysosome-specific probes bearing pH-insensitive emission, large Stokes shift and high resistance to photobleaching are highly desirable for real-time monitoring the whole process of autophagy. Fluorophores with AIE feature are capable to monitor the autophagy owning the merits of large Stokes shift and high photostability.

Guiding by the affinity of morpholine to lysosome, our group rationally designed and easily synthesized an AIEgen-based lysosome-specific probe **7** by introducing morpholine moiety into AIE-active skeleton (Fig. 2A) [49]. **7** exhibited both excited-state intramolecular proton-transfer (ESIPT) and AIE features. Thanks to the morpholine, **7** can specifically target to lysosome in HeLa cells. Because of the synergistic effect of ESIPT and AIE, the lysosomes were clearly visualized with high contrast by **7**. Through the photophysical properties investigation and cell-related experiments, the results demonstrated that **7** possesses the advantages of large Stokes shift, excellent photostability and high specificity towards lysosome, which enables its potential utility in long-term monitoring the lysosome-involved biological processes.

Long-term monitoring of autophagy has been well realized based on **7**. Rapamycin is a drug that can induce autophagy in HeLa cells [50]. The number, size and acidity of the lysosome will increase after rapamycin treatment. Under fluorescence microscope, the lysosomes were clearly visualized in the format of yellow spots after treating the HeLa cells with **7** in the presence of rapamycin

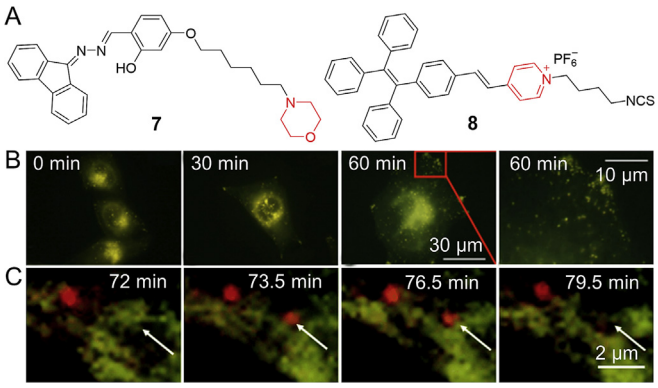

Fig. 2. (A) Structures of lysosome tracker, AIE-LysoY (**7**) and mitochondrion probe, TPE-Py-NCS (**8**). (B) Fluorescent images of **7** (10 μM) stained HeLa cells after rapamycin treatment (50 μg mL^{-1}) at different time (0–60 min). (C) Confocal images of HeLa cells co-stained with **8** (5 μM, yellow) and LysoTracker Red DND-99 (150 nM, red) in the presence of rapamycin (50 μg mL^{-1}). Time points (min) were selected from the onset and completion of the mitophagy process. Images are taken from Refs. [49,55] with permission. (For interpretation of the references to colour in this figure legend, the reader is referred to the web version of this article.)

(Fig. 2B). With prolonged rapamycin treatment, the amount and emission intensity of yellow spots were increased, indicating that the lysosome increased in amount and fused with autophagosome to form autolysosome during the autophagy. The high lysosome-specificity and superior photostability of **7** enable the clear monitoring of continuous autophagy processes on site, providing an efficient tool for deep investigation of autophagy.

As another essential process, mitophagy refers to specific autophagic elimination of dysfunctional mitochondrial degradation for maintaining cell health [51]. Development of fluorescence imaging techniques for tracking the mitophagy process could aid in better mechanistic understanding of the mitophagy. Recently, AIE probes for mitochondria have been rapidly developed and have been utilized in studying mitochondrial events [52–54]. Decoration of positively charged moieties to AIE skeleton is the most widely used design strategy to specifically target mitochondrion. However, their specificity was lost when the micro-environmental changes such as mitochondrial membrane potential (MMP) disruption, membrane depolarization and local acidification occur during mitophagy [51]. Therefore, mitochondrion-specific AIE probes with high tolerance to micro-environmental variations are critical to monitor mitophagy process. Our group has synthesized an AIEgen **8** with an isothiocyanate moiety (NCS) as shown in Fig. 2A [55]. **8** could be used as bioprobe to selectively stain mitochondria in the manner of bioconjugation between NCS and the amino groups on mitochondrial proteins, which enables **8** to possess high resistance to micro-environmental changes of mitochondria. Indeed, the emission of **8** is preserved even through the stained fixed cells were treated with organic solvents. As such, **8** could serve as a promising candidate for real-time monitoring of mitochondrial changes in the mitophagy process. As shown in Fig. 2C, **8** with yellow emission and LTR with red emission were used to co-stain HeLa cells for visualizing the process of mitophagy induced by rapamycin. Before 72 min, no obvious variation with yellow and red emission observed in mitochondria and lysosome, respectively. At 73.5 min, a new red fluorescent spot emerged (white arrow) and overlapped with the mitochondria, implying the formation of acidic autophagosome and initiation of the mitophagy process. This process is completed associating with the disappearance of the red spot at 79.5 min. The mitochondria were hydrolytically degraded by autophagosome with the weaker yellow emission at the region overlapped with the red spot. With the merits of superior photostability, good mitochondrion-specificity and high tolerance to micro-environmental changes, **8** exhibited outstanding performance in real-time monitoring of the mitophagy process, demonstrating its potential in further studying the changes of mitochondrial morphology and dynamics.

Mitochondrion with double membrane-bounded is a considerable organelle for energy supply in all eukaryotic organisms [7]. Mitochondrial morphology and dynamics are closely related to lots of functionalities, and ensure regulated metabolite supply and cell viability. Many severe diseases such as cancer, cardiovascular diseases, genetic and environmental metabolic diseases and neurodegenerative diseases are associating with the disorder of mitochondrial dynamics [7]. Therefore, high-resolved monitoring of mitochondrial dynamics has revealed that functional and structural alterations in mitochondrial morphology are important factors in pathologies and useful for therapy in modern medicine.

Traditional fluorescent techniques suffer the limited resolution due to the diffraction limit (~200 nm), which makes the structural details in mitochondrial dynamics are not sufficient enough to distinguish. Emerging super-resolution imaging techniques that break the diffraction limit have become a powerful tool for visualizing intracellular structures and monitoring subcellular dynamics in nanometer scale [21]. Thus they promise significant potential for the investigation of mitochondrial morphology and dynamics in high precision. These techniques reply on particular fluorophores with photoactivatable and photoswitchable properties. Widely used photoactivatable and photoswitchable fluorophores encountering ACQ effect will decrease their performance on super-resolution imaging. To explore new AIE probes with good performance, we and other research groups have developed a series of AIEgens for super-resolution imaging recently [56–58].

o-TPE-ON+ (**9**) was newly designed by us (Fig. 3A), which exhibits excellent photoactivation behavior [56]. **9** displayed negligible emission in aqueous solution due to the consumption of excited state energy by intramolecular rotations and twisted intramolecular charge-transfer (TICT) effect. Under light irradiation, **9** went through an unconventional photocyclodehydrogenation reaction, turning it from a weak fluorophore to a strong cyclized emitter. The cyclized emitter possessed high quantum yield, long excitation wavelength of above 500 nm and pH/environment-insensitive fluorescence, which are highly desirable in biomedical imaging. This kind of photoactivatable fluorescence turn-on behavior of **9** was demonstrated to rapidly and efficiently carry out in both fixed and live HeLa cells. Single-molecule fluorescence imaging experiment demonstrated that **9** can spontaneously blink under physiological conditions with the merits of higher photon counts, lower on-off ratio and higher precision than MitoTracker orange (MTO). Mitochondria were clearly observed from stochastic optical reconstruction microscopy (STORM) based on **9** under physiological condition, exhibiting the high resolution of 104 nm, which is much higher than that from wide-field fluorescence microscopy with the precision of 660 nm (Fig. 3B). Remarkably, no additive is required for **9**, while additives such as thiols and oxygen-scavenging agents are necessary for most used organic fluorescent probes, thereby greatly simplifying the experimental operation and allowing the live-cell super-resolution imaging of mitochondria in nanoscale. The super-resolved observation of dynamic fission and fusion processes of mitochondria was clearly presented by green and red arrowheads in Fig. 3B, respectively, fully demonstrating the promising potential of **9** for live-cell super-resolution monitoring of the change of mitochondrial morphology and dynamics in nanoscale level.

Another mitochondrion-specific AIE probe, MitoRed AIE (**10**, Fig. 3A), was further developed for live-cell direct stochastic optical reconstruction microscopy (dSTORM) to investigate the changes in

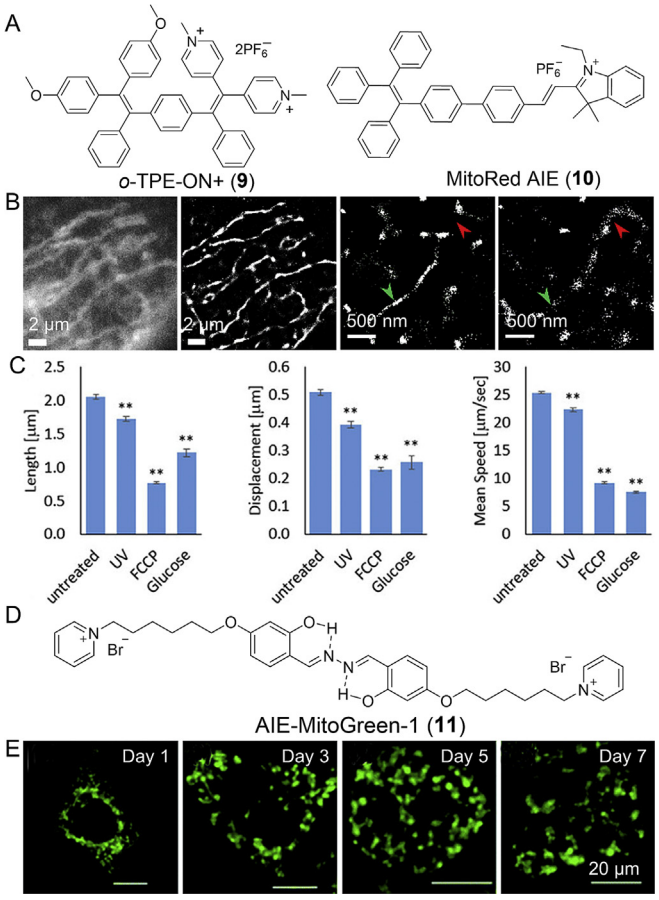

Fig. 3. (A) Structures of mitochondrion-specific AIE probes, *o*-TPE-ON+ (**9**) and MitoRed AIE (**10**) for super-resolution imaging. (B) (Left) Super-resolution imaging of mitochondria in HeLa cells stained with **9**: wide-field fluorescence microscopy image with totally blurred structure and stochastic optical reconstruction microscopy (STORM) image with clear structure below diffraction limitation. (Right) Mitochondrial dynamics in HeLa cells stained with **9**: fission (green arrowheads) and fusion (red arrowheads) events. (C) Comparison of single molecule tracks in healthy and compromised mitochondria based on **10**: all directional parameters (track displacement, length and mean speed) decrease in fragmented mitochondria (treated with UV, carbonylcyanide *p*-triflouromethoxyphenyl-hydrazone (FCCP), glucose) compared to healthy mitochondria (untreated). **Indicates statistical significance with $p < 0.01$. (D) Structure of mitochondrion-specific AIE probe, AIE-MitoGreen-1 (**11**). (E) Fluorescent imaging of differentiating brown adipose cells stained with **11** (5 μM) from Day 1 to Day 7. Images are taken from Refs. [56,57,60] with permission. (For interpretation of the references to colour in this figure legend, the reader is referred to the web version of this article.)

mitochondrial membrane motility for the evaluation of local mitochondrial membrane fluidity [57]. As **10** primarily located on membrane, the changes in membrane dynamics could affect the mobility of probe **10**, which enables observation and assessment of mitochondrial membrane fluidity by tracking single molecules in healthy and compromised mitochondria. As Fig. 3C suggests that mitochondrial impairment was induced by various methods, such as exposing mitochondria to high-power 405 nm laser until full fragmentation was observed, treating with carbonylcyanide *p*-triflouromethoxyphenyl-hydrazone (FCCP) depolarizing mitochondria, and exposing mitochondria to high concentration of glucose (50 mM) to mimic hyperglycemia and induce mitochondrial ROS production. For all these three impairment conditions, a significant decrease was observed in mobility-dependent parameters such as track length, displacement and mean speed compared to healthy mitochondria, indicating lower membrane mobility in compromised mitochondria. In comparison, no change is observed in healthy and fragmented mitochondria stained with MitoTracker Deep Red (MTDR), a commercial mitochondrial probe for STORM. All these recent results demonstrated that AIE probes **9** and **10** performed better in super-resolution imaging compared to traditionally used probes due to the inherent merits of AIEgens, which will not only extend the application of AIEgens but also provide new opportunities for super-resolution imaging.

Differentiation process of brown adipose cells has been closely related to treatment of obesity-related diseases, such as type II diabetes, atherosclerosis and cardiovascular diseases [59]. During the differentiation of brown adipose cells, their mitochondrial activities will increase to supply the larger metabolic demands, thus it is necessary to investigate the mitochondrial changes in mitochondrion-involved cell differentiation. The fluorescent monitoring of the variations in mitochondrial contents such as number, morphology and distribution could provide a non-invasive approach to identify the differentiation stages of brown adipose cells. Our group designed a mitochondrion-targeting fluorescent probe, AIE-MitoGreen-1 (**11**) by the combination of the AIE-active salicyladazine fluorophore and positively charged pyridinium groups through alkyl chain (Fig. 3D) [60]. **11** underwent both AIE mechanism via restriction of intramolecular rotation around the N-N bond and ESIPT process through intramolecular hydrogen bonds, which make **11** non-emissive in dilute solutions but highly emissive when aggregated. The AIE characteristic of **11** enabled it to emit brightly in mitochondria without self-quenching effects. Meanwhile, **11** was demonstrated to possess large Stokes shift, cell permeability, low background signal, good cellular retention, excellent photostability and low cytotoxicity. All merits make it capable to continuously monitor mitochondria changes in real-time without washing steps in brown adipose differentiation. As suggested in Fig. 3E, **11** was added to the differentiation media at day 1, 3, 5, and 7 to visualize the mitochondria number and morphology changes during the differentiation process. The mitochondria displayed tubular and reticular morphologies at the day 1 and 3. At the day 5 and 7 of differentiation the mitochondria appeared as punctate morphology. Control experiment was further carried out using undifferentiating HeLa cells stained with **11**, showing that their mitochondria were always presented as a reticular network from day 1–5, which indicates that the mitochondrial network changes are indeed caused by the differentiation process. Collectively, these results have shown that **11** is a highly suitable imaging agent for directly monitoring the changes of mitochondria morphology during the cell differentiation to identify the differentiation stages of brown adipose cells in a quick and easy manner.

Mitosis as a part of cell cycle for the maintenance of the chromosomal set occurs in cell development and growth, cell replacement, regeneration, and so on [61]. The process of mitosis divides into five stages corresponding to the completion of one set of activities and the start of the next. These stages are prophase, prometaphase, metaphase, anaphase, and telophase. Mitotic errors happened during mitosis can induce abnormal cell apoptosis or cause mutations, which may lead to cancers [61]. Therefore, monitoring of the mitosis process will not only help scientists deeply understand the mechanism of mitosis but also benefit the insight into mitosis-related diseases. To achieve such monitoring, rational designed probes are required. Because DNA and RNA are the basic elements in mitosis, fluorescent probes that have capability to specifically bind to DNA and RNA could be promisingly utilized to visualize the process of mitosis. Traditional nucleic acid probes such as ethidium bromide (EB) and its derivatives have strong affinity to nucleic acids [62], however, it belongs to strong mutagen or carcinogen. Recently, many groups have developed better and safer AIE-active probes for the quantitative detection of

nucleic acids [63–67].

Two AIE-featured probes, TTAPE-Me (**12**) and TTAPE-Et (**13**), have been designed for nucleic acid detection and mitosis monitoring by our group (Fig. 4A) [68]. **12** and **13** exhibited good water-solubility with the aid of four positively charged ammonium moieties. Due to the electrostatic interaction, the nonemissive **12** and **13** in aqueous solution were induced to intensely emit upon treated with DNA/RNA. Furthermore, **12** and **13** can selectively labeled the chromosomes and nuclei in fixed cells, which provides an opportunity for the monitoring of cell mitosis in a simple and fast manner. As displayed in Fig. 4B, onion root-tip cells in different phases of mitotic cell division can be clearly observed by the emission from **12**. In the interphase intact nuclei were clearly visualized. When entering the prophase, the nuclear membrane disintegrated and released the chromosomes into the surrounding cytoplasm. These chromosomes regularly aligned along the center plane in the metaphase and the probe **12** was induced to aggregate on the chromosomes, leading to highly emit. At anaphase, the sister chromatids migrated toward the opposite poles of the cells. And at last in the telophase, the chromosomes clustered together to facilitate the formation of a new nuclear membrane. Because **12** and **13** are practically non-emissive in the aqueous solution, the whole monitoring process was wash-free with extremely low background interference.

Long-term cellular tracing is of great scientific value and has important practical implications, for such tracing enables researchers to systematically and continuously monitor biological processes, pathological pathways and therapeutic effects [28]. Fluorescent techniques based on fluorophores such as fluorescent proteins, small organic fluorescent probes, quantum dots and fluorescent polymers have been widely used as an efficient approach for long-term cellular tracing [28]. However, these conventional fluorescent trackers with ACQ characteristics have intrinsic limitations of possible interference with stem cell differentiation, heavy metal cytotoxicity, and self-quenching at high concentration [23–26]. Because AIEgens have advantages of high brightness, strong anti-photobleaching ability, large Stokes shifts, and low cytotoxicity, they could act as highly suitable trackers for long-term cellular tracing [69–72].

Bone marrow-derived mesenchymal stem cells (BMSCs) have been demonstrated to be an efficient therapy approach for repair of bone defects caused by injuries or diseases [73]. A probe with the capability of long-term tracing of the distribution and differentiation process of delivered BMSCs could largely improve the efficiency of stem cell-based therapy. We recently developed red-emissive AIE-Tat nanoparticles for long-term tracing of the differentiation process of mouse BMSCs (Fig. 5A) [74]. The AIE-Tat nanoparticles were pre-prepared using DSPEPEG$_{2000}$, DSPE-PEG$_{2000}$-maleimide and AIEgen PITBT-TPE (**14**), further modified by a cell penetrating Tat peptide to generate AIE-Tat NPs with high quantum efficiency of 23.5%, large Stokes shift of 162 nm, high targeting ability, good biocompatibility, and excellent photostability, greatly favoring their bioimaging applications in term of high signal-to-noise ratio and low biological background. Consequently, AIE-Tat NPs exhibited higher *in vitro* tracking ability for mouse BMSCs than commercial Qtracker 655 labeling kit. As indicated in Fig. 5B, AIE-Tat NPs-labeled BMSCs have much brighter emission than Qtracker 655-labeled ones. After subculture for 6 passages, the AIE-Tat NPs labeled BMSCs still retain intense emission, but negligible emission could be observed for Qtracker 655 labeled BMSCs. This result suggested that AIE-Tat NPs possess efficient cell uptake and long-term intracellular retaining abilities. Therefore, AIE-Tat NPs are promising for the stem cell tracing in the bone repair process.

Apoptosis that refers to programmed cell death plays a critical role in cell growth and its dysregulation may lead to cancers and neurodegenerative diseases [9]. Besides, studies on apoptosis can also provide valuable diagnosis information on therapy, which has potential implications in modern biomedicine. Many efforts have been devoted to the development of fast and reliable approaches to elucidate the apoptotic process, such as laddering of DNA fragmentation [75], caspase activation [76], and externalization of phosphatidylserine (PS) [77]. PS externalization on the surface of cells in early apoptotic stage priors to the occurrence of DNA fragmentation, thus specifically targeting PS with fluorescent labels can be utilized to monitor early-staged apoptosis. Annexin V probe is an example. But this probe is unstable and suffers from the short preservation period and calcium dependence [78]. Fluorophores conjugated with zinc-dipicolylamine (ZnDPA) complexes have been developed to selectively recognize PS-rich membranes based

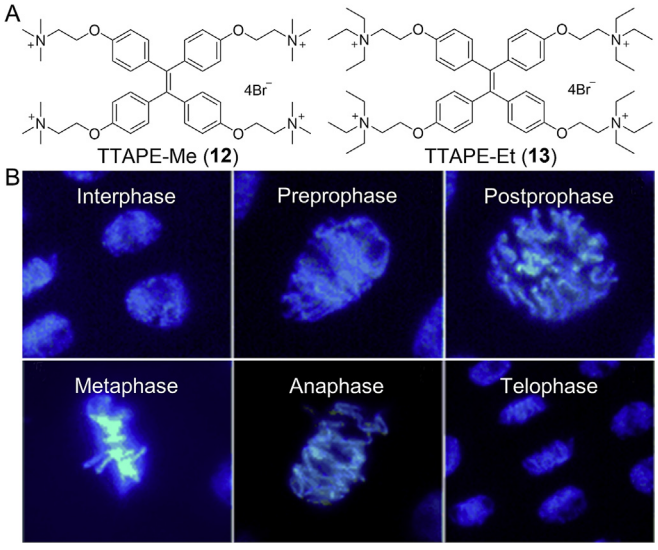

Fig. 4. (A) Structures of nucleic acid detection probes, TTAPE-Me (**12**) and TTAPE-Et (**13**). (B) Fluorescent images of cells from onion root tips at different stages of the cell cycle stained by **12** (50 μM). Image is taken from Ref. [68] with permission.

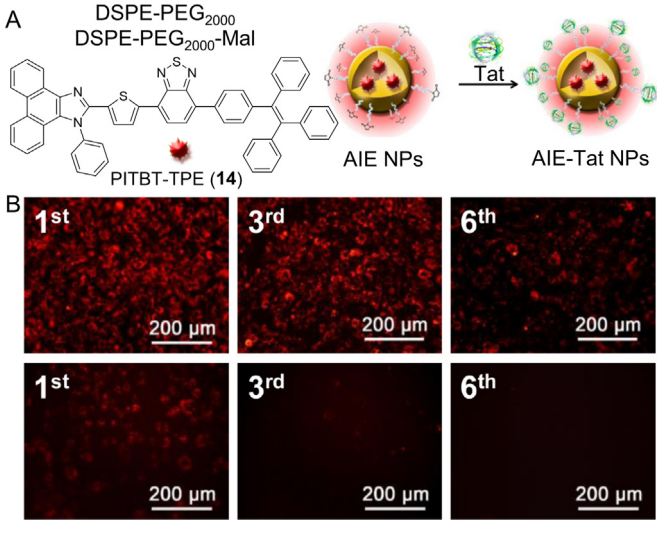

Fig. 5. (A) Structure of PITBT-TPE (**14**) and fabrication of AIE-Tat NPs based on **14**, DSPE-PEG$_{2000}$ and DSPE-PEG$_{2000}$-Mal. (B) The fluorescent images of mouse BMSCs stained with AIE-Tat NPs (Up) and Qtracker 655 (Down) during designated passages. Image is taken from Ref. [74] with permission.

on the specific binding between ZnDPA and PS [79]. However, most of them encountered small Stokes shifts and notorious ACQ effect. Also, they hardly differentiate early and late stages of cell apoptosis.

To monitor cell apoptosis in both early and late stages continuously, two AIEgens **15** and **16** decorated with ZnDPA have been designed, and show large Stokes shift, high brightness and turn-on fashion (Fig. 6A) [80,81]. As shown in Fig. 6B, due to the turn-on feature of **15**, the fluorescence background of HeLa cells is very low and signal-to-noise ratio is high at 0 min before apoptosis occurs. After treatment with staurosporine (STS) or hydrogen peroxide (H_2O_2), the apoptosis was induced. At the early stage of apoptosis, PS started to externalize on the membrane. The PS-rich cell membranes became emissive as **15** anchored on it. From 0 to 15 min, the fluorescence intensity increased gradually. Through the whole process, it was clear to observe that **15** can pass through the cell membrane, enter into the cell nuclei and interact with DNA to emit brightly when cells undergo late stage apoptosis. Moreover, **15** can also be applied to quantitatively detect real-time imaging of STS- and H_2O_2-induced cell apoptosis. Compared to annexin V, **15** and **16** have capacity to distinguish the early and late stages apoptosis.

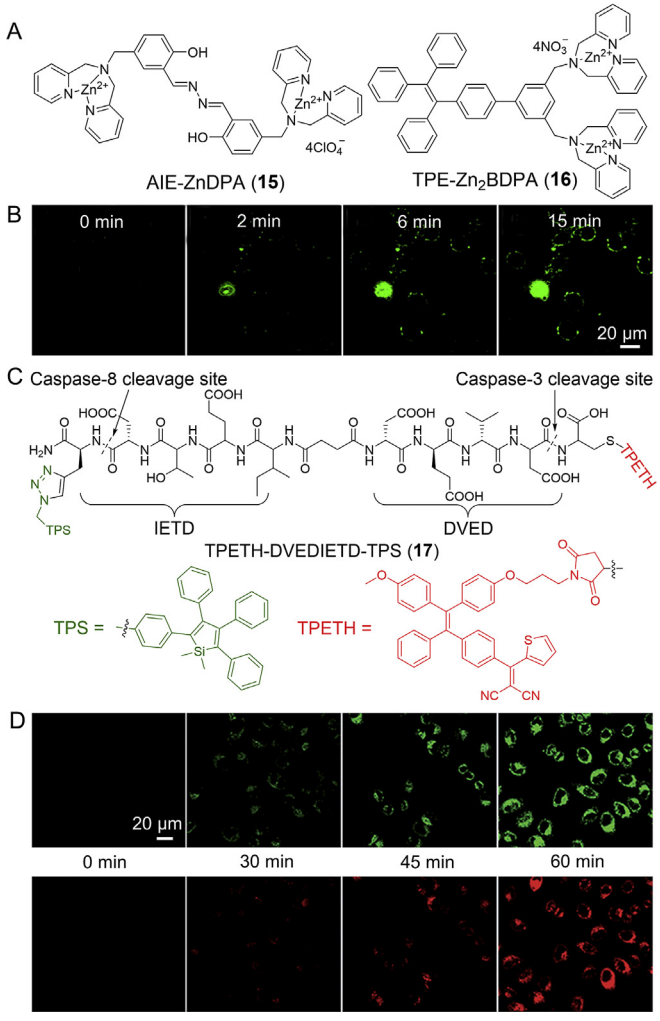

Fig. 6. (A) Structures of cell apoptosis probes: AIE-ZnDPA (**15**) and TPE-Zn_2BDPA (**16**). (B) Real time fluorescent imaging of HeLa cells induced by anticancer drug staurosporine (STS, 2 μM) for 2 h, followed by the addition of AIE-ZnDPA (20 μM). (C) Structure of caspase-responsive probe TPETH-DVEDIETD-TPS (**17**). (D) Confocal images of HeLa cells incubated with **17** (10 μM) for 2 h and further treated with H_2O_2 for different time. Green fluorescence (TPS residue, Ex: 405 nm, Em: 505–525 nm); red fluorescence (TPETH residue, Ex: 405 nm, Em: > 650 nm). Images are taken from Refs. [80,81,84] with permission. (For interpretation of the references to colour in this figure legend, the reader is referred to the web version of this article.)

Caspases play crucial roles during the apoptosis process, which involve a family of enzymes at different stages and pathways [76]. The initiator caspases (e.g. caspase-8 or -9) activate the effector caspases (e.g. caspase-3) which will ultimately lead to cell apoptosis. Because many anticancer drugs exert their anticancer effects on cancer cells through apoptosis, the monitoring of the cascade caspase activation is of practical value for diagnose diseases and evaluate the therapeutic effects of drugs. Up to now, various fluorescent probes for monitoring of multiple caspase activities have been reported [82,83]. Simple and simultaneous monitoring based on a single fluorescent probe could largely simply the procedure for biological and clinical researches. Liu et al. developed a single fluorescence turn-on probe TPETH-DVEDIETD-TPS (**17**) [84]. The two AIE-active moieties TPETH and TPS emitted red and green colors under excitation of 405 nm, respectively (Fig. 6C). Peptide DVEDIETD contained IETD and DVED which are the substrates of caspase-8 and caspase-3, respectively. Due to the superior hydrophilicity, HeLa cells only treated with **17** was almost non-emissive. Upon treated with H_2O_2, the cell apoptotic state was induced and DVEDIETD could be cleaved by the cascade caspase-8 and caspase-3, then the green fluorescence from TPS unite and the red fluorescence from TPETH moiety were sequentially lit up. This could be attributed to the processes that procaspase-8 is activated by H_2O_2 to form caspase-8 and then continuously activate procaspase-3 to caspase-3 (Fig. 6D). The fluorescence changes of **17** responsive to the caspases activity could also be used to evaluate the therapeutic efficiencies of anticancer drugs. This design strategy can be generalized to other enzyme probes simply by changing the substrate sequences, thus, it opens new ways for multiplexed diagnosis, imaging and drug screening applications.

3. Diagnosis of diseases

Collectively, for monitoring of abovementioned bioprocesses involving autophagy, mitophagy, mitochondrial morphology change and dynamics, cell differentiation, mitosis, long-term cellular tracing and apoptosis, AIEgen-based probes could serve as alternatives of commercial fluorescent probes and performed better, which is attributed to their excellent merits of large Stokes shift, high efficient emission, superior photostability, and good biocompatibility. These successful examples will inspire researchers to develop more AIE-active probes for monitoring of various essential biological processes, especially diseases-related biological processes. As we known, most diseases occurred are caused by the disorder of physiological functionalities during biological processes [10–12]. The simple, fast and sensitive diagnosis of diseases is of considerable importance for human being health. Therefore, development of fluorescence probes for precise diagnosis of diseases is highly desirable. AIEgens have been widely demonstrated to afford the superior behaviors in fluorescence imaging, thus AIEgen-based probes will act as ideal agents for diagnosis of various diseases such as cancer, inflammation, blood brain barrier damage, and so forth.

Cancer, as the leading cause of mortality worldwide, seriously threatens the health of human being and the incidence of cancer is continuously increasing [10]. Enormous efforts have been devoted to be insight into cancer and lots of new techniques as well as effective anticancer drugs have been developed for diagnosis and treatment [15–18]. Among them, early diagnosis and therapy of cancer before its metastasis could largely increase the cure rate, thus attracts much attention. However, the small size of tumor is difficult to observe, making the early diagnosis difficult. Fluorescent

techniques can realize the real-time monitoring with high resolution, which endows them unique superiorities in diagnosis of cancer on the early stage. Thus, a lot of fluorophores have been developed for the early-stage diagnosis of cancers [28]. However, the easy photobleaching and notorious ACQ effect seriously limited their further applications in long-term and continuous monitoring. AIEgens emerged as a thorough solution to address these problems will exhibit promising potential in diagnosis of cancers.

Our group has designed an AIEgen-based diagnostic system that can selectively distinguish cancer cells against normal cells by using mitochondrion-specific AIEgens [85]. TPE-IQ-2O (**18**), DPIBP (**19**) and TPE-Ph-In (**20**) are the examples and their structures are shown in Fig. 7A. Their inherent positive charges endow them with high specificity to mitochondria showing greenish-yellow, yellow and red emission. Because of the higher membrane potential difference and stronger electrostatic interaction, **18**, **19** and **20** were preferentially internalized and accumulated in cancer cells over normal cells, thus resulting in stronger emission in cancer cells. The results in Fig. 7B demonstrated this kind of differentiation. Bright fluorescence was only observed in the mitochondria of cancerous HeLa cells, while negligible fluorescence was observed in COS-7 cells. Apart from HeLa and COS-7 cells, the differentiation between different cell lines (cancerous cells: MDA-MB-231, MCF-7, PC-9, A549, HCC-827 and HepG2; normal cells: LX-2, HEK-293 and MDCK-II) stained with **18**, **19** and **20** was also successfully conduced. Further, cancerous cells (HeLa cells or MDA-MB-231 cells) could also be clearly distinguished when they co-cultured with normal cells (COS-7 cells or MDCK-II cells) together. All these results experimentally figured out the promising potential of AIEgens **18**, **19** and **20** in the early-stage diagnosis of rare cancer cells in normal tissues, and it motivated us to develop more AIEgens with long-wavelength excitation and emission for practical diagnosis of cancer cells *in vivo*.

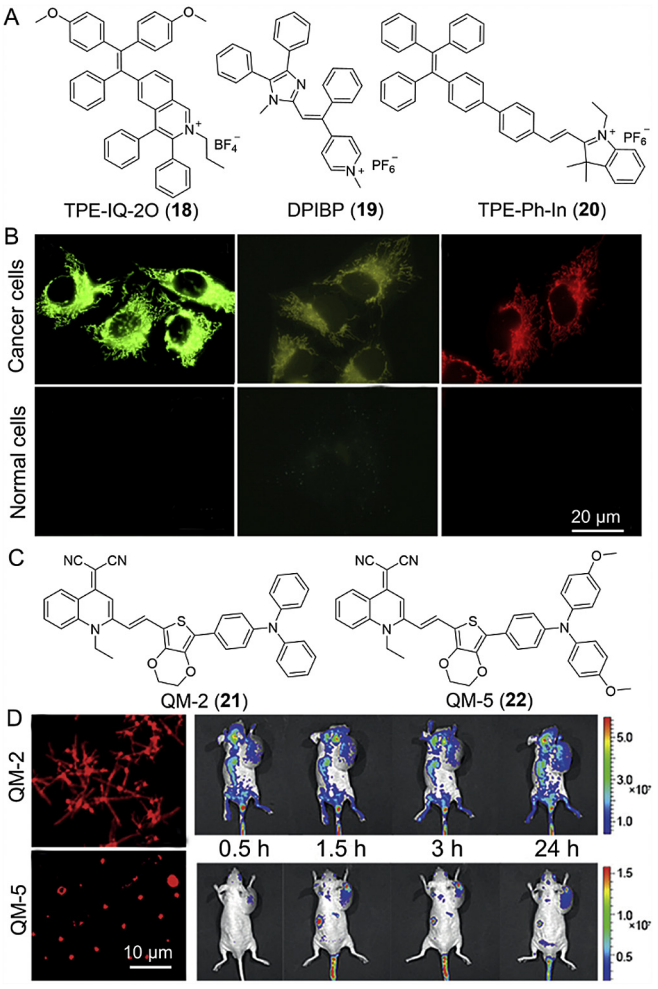

Fig. 7. (A) Structures of mitochondrion-targeting TPE-IQ-2O (**18**), DPIBP (**19**) and TPE-Ph-In (**20**). (B) Fluorescent images of differentiation of cancer cells (HeLa) from normal cells (COS-7) by **18**, **19** and **20**. (C) Structures of QM-2 (**21**) and QM-5 (**22**). (D) (Left) Confocal images of the rod-like and spherical morphologies of aggregates of **21** and **22**, respectively. (Right) *In vivo* non-invasive imaging of tumor-bearing mice after intravenous injection of nanoaggregates of **21** and **22** at different periods of time (0.5, 1.5, 3 and 24 h). Images are taken from Refs. [85,86] with permission.

For highly-efficient diagnosis of cancer *in vivo*, the development of far-red and near-infrared (NIR) emissive AIEgens that can distinguish tumors from normal tissues are of great concern. Zhu et al. designed an AIE-active NIR system by employing the quinoline-malononitrile (QM) as the AIE building block [86]. Two representative examples, named QM-2 (**21**) and QM-5 (**22**), exhibited NIR emission above 650 nm (Fig. 7C), which could enable deep tissue penetration, avoid the autofluorescence of biosubstrates as well as minimize photo-damage to living cells. **21** and **22** could form different morphologies when they aggregated. As shown in Fig. 7D, **21** was apt to form rod-like microstructures while **22** tended to aggregate to the sphere-shaped nanoparticles. The different shapes of aggregates for **21** and **22** were ascribed to their unique molecular structures. Notably, the different shapes could exert their own effect on tumor-targeted imaging *in vivo*. Upon intravenous injection of **21** into the mice, **22** aggregates rapidly distributed in the whole mouse body via the blood circulation. Even at 24 h after the injection, the **21** aggregates did not distribute specifically in tumor. However, the distinct NIR fluorescence of **22** aggregates could predominately located in the tumor rather than other organs, and the emission can retain in tumor tissue even at 24 h after injection (Fig. 7D). This result may be due to the enhanced permeability and retention (EPR) effect of spherical **22** aggregates. This work makes it clear that the relationship between the morphologies of AIE nanoaggregates and the tumor targeting *in vivo*. The spherical morphology of AIE nanoaggregates has a better tumor targeting than the rod-shaped, which will guide researchers to develop better nanoparticle-based AIE systems for efficient diagnosis of cancer.

Accurate diagnosis of cancer cell types will facilitate precisely targeted therapy, which gives higher treatment efficiency and lower side effects compared to non-specific traditional cancer therapy [87]. Fluorescent probes or nanoparticles, conjugated with tumor-specific biomarkers such as antibodies, cRGD, streptavidin, folic acid and Tat peptide, are especially suitable for such accurate diagnosis of cancer with advantages of superior brightness, easy decoration and high resolution [88]. Thus, AIEgen-based probes and nanoparticles could exert their great potential on accurate diagnosis of cancer and many researches have been reported. Recently, Wei and Tang et al. have designed two kinds of red-emissive AIEgens *t*-BuPITBT-TPE (**23**) and DPPBPA (**24**) (Fig. 8A) [89,90], and proposed the general procedure for targeting groups-decorated AIEgen nanoparticles (TG-AIEgen-NPs) for selective differentiation of different types of cancer cells (Fig. 8B). **23** was encapsulated into biocompatible DSPE-PEG and then decorated with a monoclonal antibody cetuximab (C225). The obtained **23**-C225-NPs can be used for targeted imaging of non-small cell lung cancer cells with an overexpressed epidermal growth factor receptor (EGFR-positive) over EGFR-negative cells. The specific targeting ability of **23**-C225-NPs has been well verified by confocal microscopy. **23**-C225-NPs were efficiently internalized into EGFR-positive HCC827 cells, and thus the cells showed a strong red fluorescence. In a sharp contrast, a very weak fluorescence was

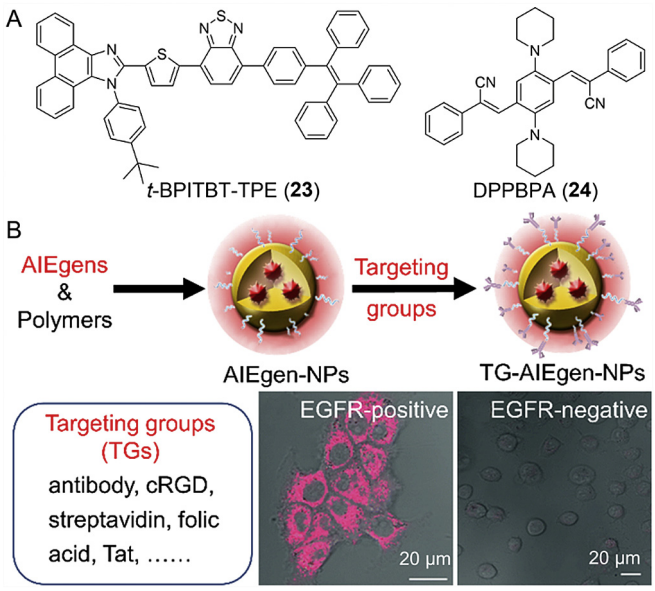

Fig. 8. (A) Structures of red-emissive AIEgens: *t*-BPITBT-TPE (**23**) and DPPBPA (**24**). (B) General fabrication method for TG-AIEgen-NPs with targeting groups (TGs) for cancer cells, and the confocal laser scanning microscope images of EGFR-positive HCC827 and EGFR-negative H23 cells after incubation with **23**-C225 NPs at 37 °C for 8 h. Images are taken from Refs. [89,90] with permission. (For interpretation of the references to colour in this figure legend, the reader is referred to the web version of this article.)

observed in EGFR-negative H23 cells. These results clearly demonstrated that **23**-C225-NPs are excellent fluorescence imaging agents for precisely targeted imaging of EGFR-overexpressed cells with significant advantages of highly efficient red emission, good biocompatibility and excellent photostability.

Because the diagnosis of cancers is conducted *in vivo*, such as preclinical murine models, the biodistribution and biosafety of AIEgens *in vivo* must be of great concern. Abovementioned has illustrated that the size-suitable AIEgen-based NPs would mainly distribute in tumors due to the EPR effect or the targeting ability from targeting groups on the surface of NPs. And it could be also observed the distribution of AIEgen-based NPs in major organs including heart, liver, spleen, lungs and kidney. Qian et al. have demonstrated that AIEgen-based NPs could be flowing in the circulatory system *in vivo*, and evidently observed the fluorescence of AIEgen-based NPs in all the major organs after 3 h and 6 h post-injection and then predominantly accumulated in liver as time went by for the metabolism of AIEgens upon the metabolic functions of animals [91]. With regard to the safety of PEG-encapsulated AIEgens *in vivo*, many groups have been investigating but no definite report has been published so far. However, it could be deduced that AIEgen-based NPs probably show good biocompatibility *in vivo* even if the PEG coating falls apart based on the following concerns: i) enormous examples have verified the good cell viabilities of AIEgens except AIE photosensitizers for photodynamic therapy [26–44], ii) as the major component for AIEgen-based NPs, PEG is well-known biocompatible polymers for various biological applications [92].

Closely related to major diseases such as cancer, cardiopathy, diabetes and Alzheimer's disease, inflammation has attracted great attention [93]. As an indicator of inflammation, peroxynitrite ($ONOO^-$) is generated from the reaction between nitric oxide ($^{\bullet}NO$) and superoxide ($O_2^{\bullet-}$) radicals. Therefore, selective monitoring of elevated $ONOO^-$ production at inflammatory level are undoubtedly important to the early-stage diagnosis of carcinoma and provide valuable information on elucidating the pathological process and improving therapeutic efficiency. To date, many fluorescent probes were explored for $ONOO^-$ detection but unsuitable for the practically disease-allowed detection window of $ONOO^-$ level. Recently, Ding et al. have rationally designed a fluorescence turn-on AIE nanoprobe based on AIEgen TPE-IPB (**25**, Fig. 9A) with $ONOO^-$ detection window at the pathological level and that nanoprobe could distinguish the disease site in a selective and high-contrast manner [94]. Non-emissive **25** could react with $ONOO^-$ to generate AIE-active TPE-IPH (**26**) in short time. Encapsulation of **25** with lipid-PEG_{2000} matrix yielded nanoprobe (**25**-PEG), which exhibited no emission in aqueous media while emitted intense yellow fluorescence after reacted with $ONOO^-$ at pH 7.4 (Fig. 9B). Only $ONOO^-$ can turn on the fluorescence of **25**-PEG, whereas other ROS (tert-butylhydroperoxide (TBHP), ClO^-, $^{\bullet}OH$, $ROO^{\bullet}$, $O_2^{\bullet-}$ and

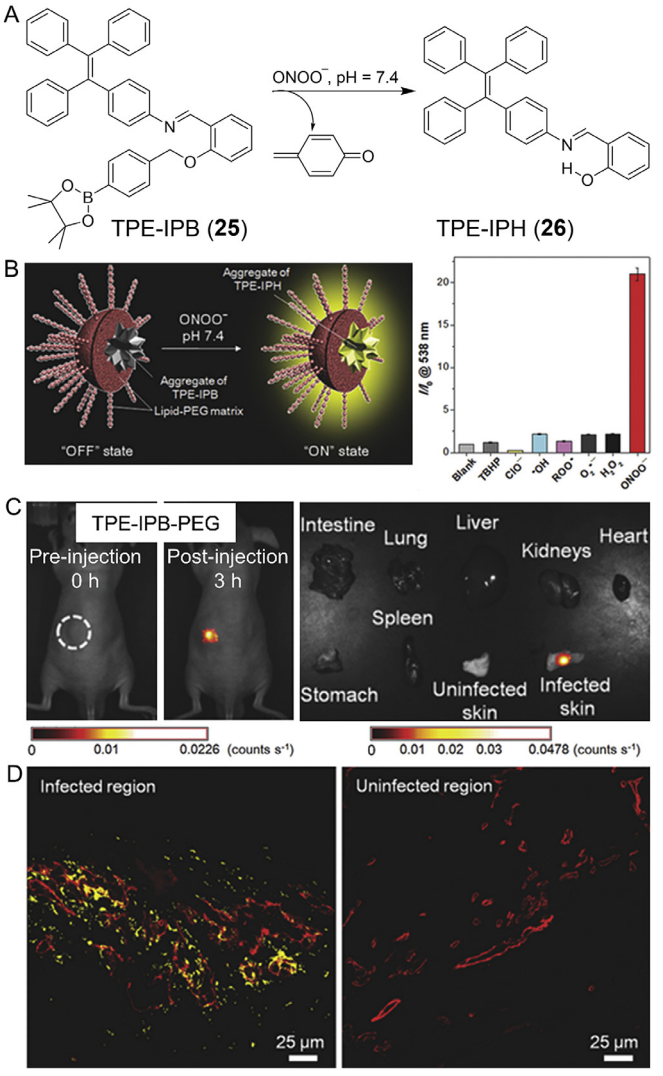

Fig. 9. (A) Structure of $ONOO^-$ probe TPE-IPB (**25**) and the resulting product TPE-IPH (**26**). (B) Schematic illustration of aggregate of **25**-PEG and the performance in the presence of $ONOO^-$. Plot of I/I_0 versus various reactive oxygen and nitrogen species (RONS) in PBS buffer (pH 7.4). I and I_0 are the PL intensities of **25**-PEG with and without RONS, respectively. (C) Time-dependent *in vivo* fluorescence images of inflammation-bearing mice before and after intravenous injection of **25**-PEG. The white circles indicate the methicillin-resistant staphylococcus aureus (MRSA)-infected region. *Ex vivo* fluorescence images of various tissues from inflammation-bearing mice after intravenous injection of **25**-PEG aggregate for 3 h. (D) Representative confocal images of slices of infected and uninfected skin tissues from **25**-PEG-treated mice. The red fluorescence represents blood vessels. Images are taken from Ref. [94] with permission.

H_2O_2) induce negligible fluorescence changes.

Immune cells such as neutrophils and macrophages will migrate to the inflammatory site, and then stimulate to release substantial amounts of RONS including $ONOO^-$ [95]. The produced $ONOO^-$ could turn on **25**-PEG fluorescence in inflammatory region. As shown in Fig. 9C, almost no fluorescence signal was detected before **25**-PEG injection, while the fluorescence at the inflammatory site turned on and became significantly intense after **25**-PEG injection for 3 h. It is ascribed that **25**-PEG is prone to accumulating to the inflammatory region by EPR effect, and reacted with $ONOO^-$ to be lit up. The excellent selectivity of **25**-PEG in the inflammation imaging was further confirmed by *ex vivo* imaging of different tissues (Fig. 9C). Besides, the infected and uninfected skins were also sliced for blood vessel staining in Fig. 9D, yellow emissive dots are clearly observed around the blood vessels (indicated by red fluorescence) in the inflammatory region, while no emission is observed in the slice of normal skins. This work provides new insights into development of advanced fluorescent nanoprobes for diagnosis of inflammatory and related diseases *in vivo*.

Blood-brain barrier (BBB) is a specialized cerebral vascular system and plays a key role in strict regulation of the paracellular permeability [96]. The damage of BBB will result in seriously negative effects even neurological diseases, and acts as a critical indicative omen of the extent of neurological damage. As a consequence, precise evaluation of the BBB integrity is significant for the assessment of injury and evaluation of therapeutics. So far, evans blue (EB) assay has been commonly used for the evaluation of BBB damage [97]. However, EB has several limitations of the lethal toxicity *in vivo* and confounding problems in quantitative assay by spectroscopic methods. A sensitive, selective, and nontoxic method for evaluating BBB damage and vascular leakage has been developed based on AIEgen NPs by Liu et al. [98].

AIE-active TPETPAFN (**27**, Fig. 10A) exhibited bright red emission in the solid state as well as good photostability and biocompatibility. **27** was used to fabricate nanoparticles (**27**-NPs) with sizes of 60, 30 and 10 nm for monitoring of BBB *in vivo*. A rat model of photothrombotic ischemia (PTI) was selected to induce the BBB damage for precise diagnosis of BBB integrity. Under this model, the 30 nm **27**-NPs were verified to be the most sensitive and selective probes for BBB damage evaluation, while the 60 nm **27**-NPs can rarely across BBB and the 10 nm **27**-NPs show poor selectivity. When the BBB was intact without PTI, no fluorescence of 30 nm **27**-NPs was observed in coronal slices, indicating 30 nm **27**-NPs cannot penetrate through the BBB (Fig. 10C). While EB exhibited leakage in the coronal slices at different areas across healthy BBB (Fig. 10B). When the BBB was treated with PTI, clear leakage could be visualized in coronal slices. Bright red fluorescence of 30 nm **27**-NPs was observed at the ischemic region in the coronal slice, while negligible emission was detected from others (Fig. 10D). In contrast, 30 nm **27**-NPs offered higher specificity than EB in monitoring the BBB leakage. In addition, due to their tunable sizes, the **27**-NPs offered new opportunities to study BBB damage under different pathological conditions and to evaluate the efficacy of various therapeutic strategies in protecting the BBB.

As reviewed above, fluorescent techniques could provide better visibility, lower cost and higher resolution, however they unavoidably suffer from the limited penetration depth, which will be detrimental for diagnosis of diseases *in vivo*. To address this problem, the assembly of fluorescent techniques and others with deep penetration could provide an effective approach. Magnetic resonance imaging (MRI) technique can act as a suitable candidate due its deep penetration and nonradiative harm [99]. Dual-modal fluorescent probes with both fluorescence and MRI signals would be perfect for the high resolution and less depth limitation for clinical diagnosis.

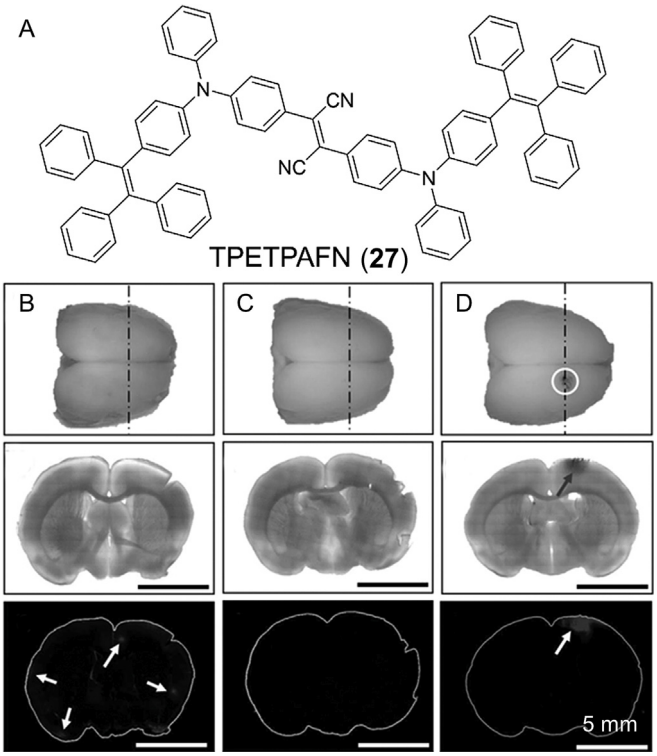

Fig. 10. (A) Structure of TPETPAFN (**27**) for evaluation of blood-brain barrier damage. (B-D) From left to right: optical microscope images (the white circles indicate the lesion regions, the dashed lines indicate the section site of coronal slices in S1FL region), confocal bright field (the grey arrows indicate the lesion regions) and fluorescence images (the white arrows indicate the fluorescence generated by the leaked **27**-NPs) of the coronal slices of the brain with administration of evans blue (EB) without photothrombotic ischemia (PTI) (B), 30 nm **27**-NPs without PTI (C) and at 3 h post PTI (D). Image is taken from Ref. [98] with permission.

Our group has developed an AIE-active dual-modal MRI contrast agent, TPE-2Gd (**28**, Fig. 11A) for both fluorescence and magnetic imaging [100]. **28** itself aggregated into micelles at a high concentration in aqueous solution, with high emission and photostability. Such feature enabled **28** as a good fluorescent probe for cell imaging. As shown in Fig. 11B, **28** was internalized into living HeLa cells through the endocytosis pathway, and the cytoplasmic regions of HeLa cells was lit up with blue emission. On the other hand, **28** possessed comparable magnetic relaxivity as the commercial Magnevist. However, **28** exhibited the longer circulation time and the higher contrast than Magnevist. As shown in Fig. 11C, the MRI signal in cardiac chambers is very weak before injection (Baseline). After injection of **28** or Magnevist for 1 min, the cardiocoelomic contrast enhanced. However, the strong MRI signal of Magnevist was decreased rapidly within 5 min and back to baseline less than 60 min, whereas the MRI signal of **28** still remained much higher than that of baseline even over 150 min. Similar results were occurred in liver. Further, the intense MRI signal in the bladder at 5 min after injection indicated that Magnevist is rapidly eliminated from body into urine, while **28** can also be accumulated in the bladder at 150 min. This long retention time could be ascribed to the slow disassembly of **28** nanoaggregates.

4. Theranostics of diseases

Before therapy, disease diagnosis is the first and critical step. Therefore, real-time monitoring of disease development is of significance for researches in medical science and therapy in clinic.

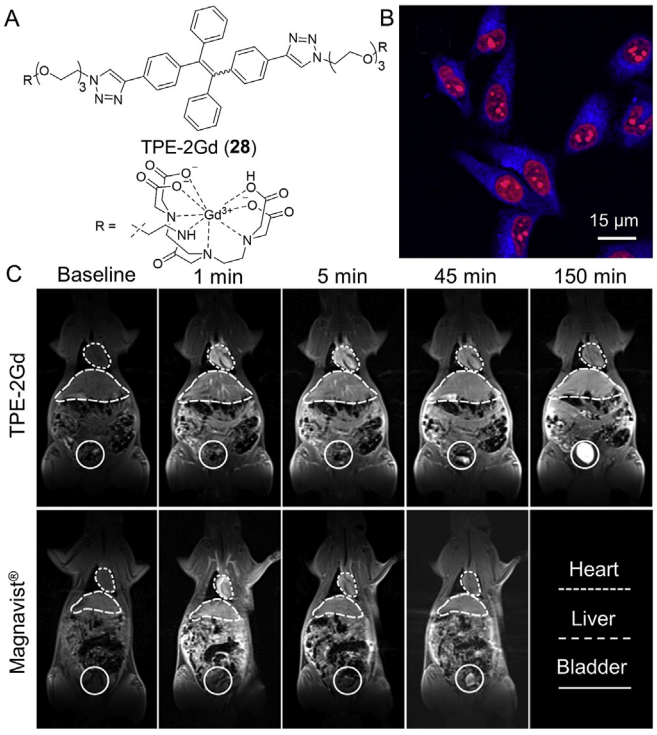

Fig. 11. (A) Structure of dual-modal AIE probe TPE-2Gd (**28**). (B) Fluorescent images of HeLa cells stained with **28** (30 μM) and PI. (C) Coronal T_1-weighted MR images of rat after intravenous injection of **28** and Magnevist with concentration of 0.1 mmol/kg Gd^{3+}. Images are taken from Ref. [100] with permission.

The work abovementioned has demonstrated that AIEgen-based probes performed well in diagnosis of various diseases. Compared to commercial available fluorescent probes, AIEgen-based probes presented lots of advantages such as anti-ACQ effect, high resistance to photobleaching and bright emission, which allow them to realize the diagnosis of diseases in the early stage. After diagnosis, efficient and precise therapy will be the next aim. If a fluorescent probe not only works for diagnosis of diseases but also acts as a therapeutic agent, it is of much interest and highly desired thereby. Theranostics is a term that was firstly proposed by researchers in 2002 [101], which combined diagnostic imaging and therapy together. As many materials possessing the functionalities of chemotherapy, photodynamic therapy (PDT) or radiotherapy, incorporation of them into different imaging agents will generate new theranostic systems for image-guided chemotherapy, PDT, radiotherapy and so on, which will make therapy under visualization and provide a useful tool to evaluate the therapeutic effect. Due to the versatile functions and exciting properties of AIEgens, it is promising to develop multifunctional AIEgen-based probes for image-guided therapies. Recently, theranostic system based on AIEgens has been developed [102–107]. Here, several representative results have been reviewed.

For cancer therapy, development of chemical drugs plays a vital role however is a time-consumed, high-risk and high-cost process. Slight difference in the molecular structures of drugs may largely affect their therapeutic effects and their pharmacodynamics is difficult to elucidate without suitable indicators [108]. Thus, the development of theranostic drugs, which combining both diagnostic and therapeutic capabilities may allow the action of drugs to be monitored visually, further being benefit for the efficacy evaluation and screening of drugs in a real-time manner. Our group has developed a simple system by modifying drugs to be AIE-active to satisfy image-guided chemotherapy [109].

Tamoxifen (TMX (**29**); Fig. 12A) is a chemotherapeutic agent for breast cancer treatment by targeting to estrogen receptor (ER). However, the cellular-level distribution and functions of **29** were unclear due to the lack of visual signal. Considering the similar molecular structure between **29** and fluorescent TPE, an AIE-active TPE-TMX (**30**) (Fig. 12A) was synthesized as a theranostic drug for breast MCF-7 cancer cells, achieving the aims of both fluorescent indicators of distribution and chemical drug of therapy. As shown in Fig. 12B, there is no fluorescence observed to be indicative of exact intracellular distribution of **29** in MCF-7 cells. In contrast, MCF-7 cells stained with **30** show intense blue emission (Fig. 12B). Through the co-staining experiment with LTR (Fig. 12B), it could be clear that **30** aggregates mainly distributed in lysosomes of live MCF-7 cells. The high brightness and excellent photostability properties of **30** endow itself with long-term cell tracing ability which enables us to visually understand how the drug distribute and interact with cells. Besides, **30** could be prone to accumulate in MCF-7 cells and induce the lysosome formation, which could bring the therapeutic effect on MCF-7 cells. As suggested in Fig. 12C, **30** exhibited comparative therapeutic efficacy to **29**. **30** was only therapeutically responsive to MCF-7 cells, and the higher the dose of **30** used, the less amount of MCF-7 cancer cells survived. The cell viabilities of other cell lines, including HeLa, Cos-7 and ER-negative MDA-MB-231 cells, changed little even at a high concentration. All of these results demonstrated that **30** could act as a promising theranostic agent for image-guided chemotherapy of ER-positive breast cancer cells, and this work tells us the development of drugs with emission will facilitate the insight into pharmodynamics and evaluation of therapeutic efficacy, effectively prompting the drug development.

As another effective approach for cancer therapy, photodynamic therapy (PDT) has recently been paid attention due to the distinct merits of precise controllability, minimal invasive nature and high spatiotemporal accuracy [110,111]. PDT refers to the process of

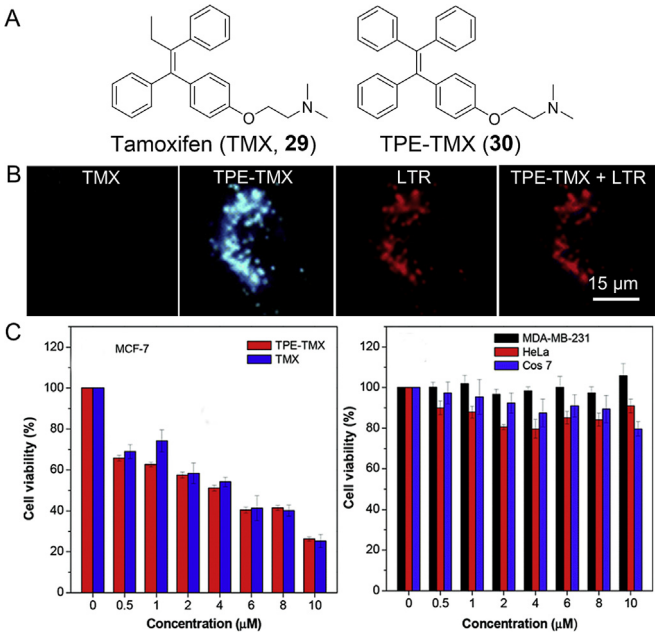

Fig. 12. (A) Structures of tamoxifen (TMX, **29**) and TPE-TMX (**30**). (B) Fluorescence images of MCF-7 breast cancer cells treated with **29** (2 μM) or **30** (2 μM) and followed by staining with LTR (50 nM) for 15 min. Ex: 330–385 nm (for **29**) and 520–560 nm (for LTR). (C) Cell viabilities: (Left) MCF-7 cells incubated with different concentrations of **29** and **30**, (Right) different cells in the presence of **30** with different concentrations. Image is taken from Ref. [109] with permission.

generation of ROS to kill cancer cells, which is normally induced by photosensitizers upon light irradiation. Two critical aspects for PDT are the ROS generation yield and light penetration. Principally, the small energy gap (ΔE_{st}) between the lowest singlet state (S_1) and the lowest triplet state (T_1) of photosensitizer facilitates intersystem crossing (ISC) process to efficiently produce ROS [31]. And the long-wavelength light used in PDT will bring deep penetration in tissues to improve the use rate of light. Additionally, the emission from photosensitizers endows the whole therapy processes with image-guidance and provides useful tools for the deep insights into the therapeutic mechanism.

Porphyrin and phenylthiazinium derivatives are the most widely used photosensitizer for PDT in clinic [110], however, their ACQ effects in emission significantly diminish the generation of ROS. Inspired by these, the design rationale that reduces the energy difference between the S_1 and T_1 would promote ISC, which could favor the transfer of the T_1 energy of photosensitizers to neighboring oxygen (O_2), producing radicals or singlet oxygen (ROS) for PDT [31]. A general approach for design of photosensitizers is introduction of strong electron donors (D) and acceptors (A) into luminogens to the low the energy of S_1 toward to that of T_1. Well-used strong electron donors and acceptors are methoxyl, amino, cyanoethylene, pyridinium, isoquinolinium, 9,10-anthraquinone, and so on. Thus, structurally linking these functional groups to AIEgens will potentially make themselves act as both imaging indicators and photosensitizers for image-guided PDT. Meanwhile, the excited states of AIEgen-based photosensitizers will not be quenched upon aggregation due to the characteristic of AIE, which efficiently addresses the issues that the emission quenching and ROS diminishing existing in traditional ACQ luminogens. In addition, the means that decoration of suitable electron donors and acceptors to AIE skeletons generates the isolated distribution of HOMOs and LUMOs would principally result in the low ΔE_{st}, thus largely facilitates the transfer from S_1 to T_1 and enhances the ROS generation efficiency of AIEgens. Consequently, AIEgen-based photosensitizers with bright emission and efficient ROS generation in aggregates have been well-designed recently as the promising agents for image-guided PDT. Considering the short lifetime (< 0.04 μs)) and limited radius of action (< 0.02 μm) of ROS [110], the distribution of photosensitizers inside cells largely affects the therapeutic effect of PDT. Mitochondria are verified as the main target of ROS and play the critical role in cell apoptosis [112], thus selective targeting toward mitochondria for photosensitizers will significantly enhance the PDT efficiency. Thus, properly designed AIEgen-based photosensitizers with mitochondrion-specificity could not only image mitochondria but also serve as photosensitizers for PDT. Many groups have developed lots of systems based on multifunctional small AIEgens and AIEgen-based nanoparticles for image-guided PDT for cancer therapy [85,102,113–117].

Isoquinolinium-based TPE-IQ (**31**, Fig. 13A) [118] that was obtained through one-pot reaction with high yield possesses excellent mitochondrion-specificity. The mitochondrial structures were clearly visualized with green emission as shown in Fig. 13C. Notably, **31** can easily enter into cell with short staining time and also works fine in fixed cells. On the other hand, **31** can generate ROS effectively upon light irradiation. As suggested in Fig. 13B, the system involving **31** and ROS indicator H2DCF-DA was initially non-fluorescent without 365 nm UV light irradiation, revealing the low dark toxicity. Upon 365 nm UV light irradiation for a short time, the emission of H2DCF-DA was gradually increased, while no or extreme weak emission was showed in the solution of either **31** or H2DCF-DA. The excellent ROS production properties of **31** facilitate the PDT of HeLa cells. Without light irradiation, the HeLa cells stained with **31** were healthy with normal morphology (Fig. 13D). After UV irradiation, the mitochondria in HeLa cells became

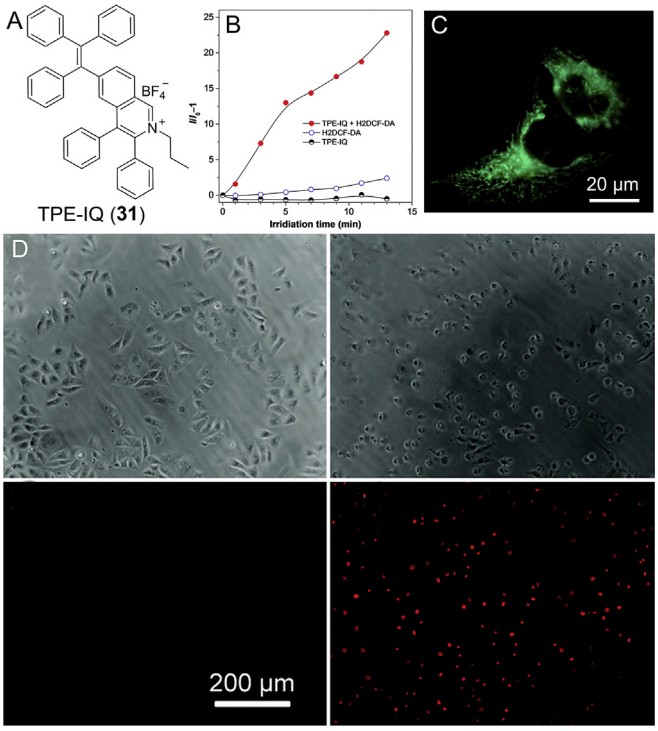

Fig. 13. (A) Structure of TPE-IQ (**31**). (B) Release of ROS monitored by ROS indicator H2DCF-DA: change in fluorescence intensity at 534 nm in the presence of **31** (10 μM), H2DCF-DA (1 μM), or their mixture in PBS upon UV irradiation (365 nm) for different time. Ex: 485 nm. (C) Fluorescence images of mitochondria in HeLa cells stained with **31** (200 nM) for 15 min. Ex: 330–385 nm. (D) Bright field and fluorescence images of PI stained (1.5 μM, 10 min) HeLa cells. After incubation with **31** for 15 min, the cells were treated without/with UV irradiation for 2 min, followed by further incubation with **31** for 12 h in the dark. Images are taken from Ref. [118] with permission.

rounded-structure and the cells look unhealthy with serious shrink and detachment from the glass substrate. Red emission from propidium iodide was also observed inside cells, indicating that the cells underwent late apoptosis and **31** can effectively kill HeLa cells.

AIEgen-based photosensitizers loading into nanocarriers favor bright emission and high ROS generation [31]. Thus, construction of multifunctional AIEgen-based nanoparticles for image-guided PDT is a recent popular research topic. AIE-featured BTPEAQ (**32**) structured with two TPE as the electron donor and 9,10-anthraquinone (AQ) as the electron acceptor has been synthesized by Liu et al. (Fig. 14A). [119]. Nanoaggregates formed by **32** solely in aqueous exhibited negligible fluorescence due to strong intramolecular charge-transfer (ICT) effect. However, polymer-shelled **32** dots based on matrix encapsulation approach exhibited much improved brightness, and the ROS generation yield was also enhanced with the value of 38%. Thus, polymer-shelled **32** dots have the capability as a promising AIEgen-based photosensitizer for image-guided PDT. To endow the cancer targeting, polymer-shelled **32** dots were further functionalized with cRGD, obtained **32**-cRGD dots can target integrin overexpressed cancer cells such as MDA-MB-231 breast cancer cells. As displayed in Fig. 14B, very bright red emission in MDA-MB-231 cells from **32**-cRGD dots can be observed, whereas very weak emission can be found inside low integrin expression HeLa and NIH-3T3 cells. Due to the unique targeting and image-guidance properties, MDA-MB-231 cells were selectively killed due to the PDT effect of **32**-cRGD dots over the normal NIH-3T3 cells. MTT assays showed the viability of MDA-MB-231 cells dramatically decreased with increase of concentration of **32**-cRGD dots under light irradiation while almost no effects to

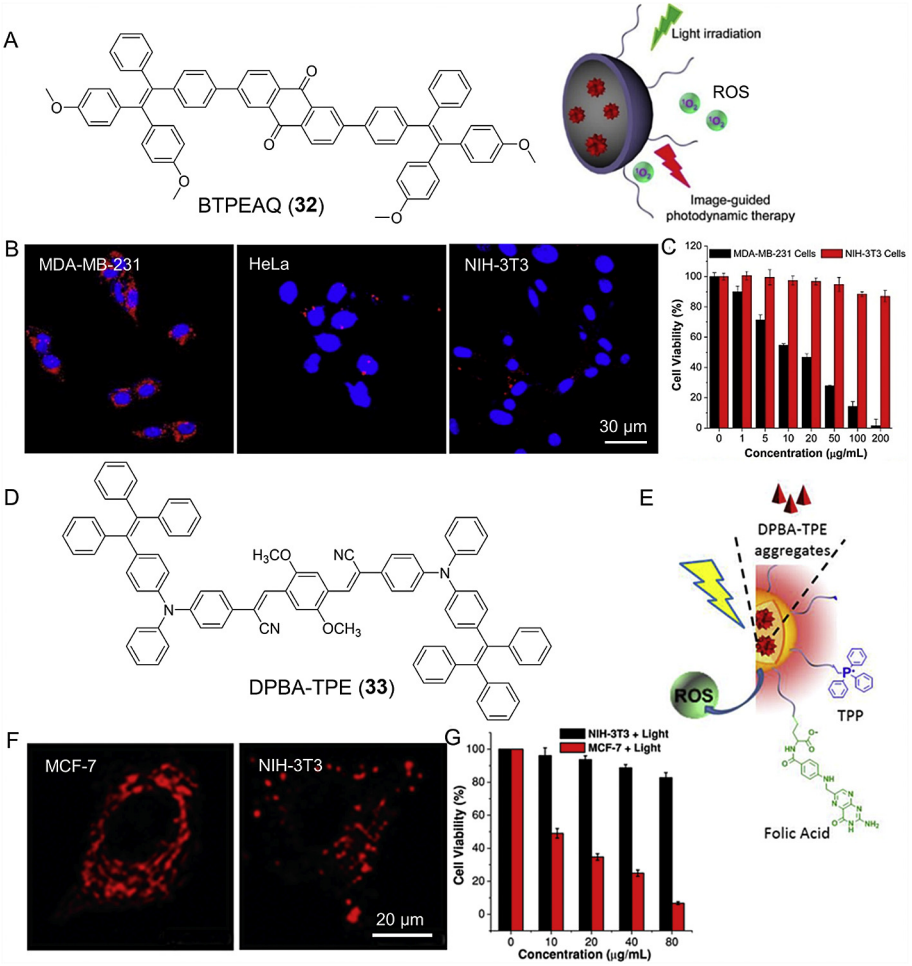

Fig. 14. (A) Structure of AIEgens BTPEAQ (**32**) and the graphic of **32**-cRGD dots. (B) Confocal images of MDA-MB-231, NIH-3T3 and HeLa cells after incubation with **32**-cRGD dots for 2 h. The nuclei were stained with Hoechst 33342 (5 μg mL^{-1}, 10 min). (C) Cell viabilities of **32**-cRGD dots treated MDA-MB-231 cells and NIH-3T3 cells with white light irradiation (100 mW cm^{-2}, 10 min). (D) Structure of AIEgens DPBA-TPE (**33**). (E) The graphic of dual-targeting FA-**33**-TPP dots. (F) Confocal images of folate receptor (FR)-positive MCF-7 cancer cells and NIH-3T3 normal cells after incubation with FA-**33**-TPP dots (20 μg mL^{-1}). Ex: 543 nm, Em: > 650 nm. (G) Cell viabilities of MCF-7 cancer cells and NIH-3T3 normal cells after incubation with FA-**33**-TPP dots at varied concentrations, followed by white light irradiation (250 mW cm^{-2}). Images are taken from Refs. [119,120] with permission.

NIH-3T3 cells (Fig. 14C).

Besides the design of AIEgen-based nanoparticles for specific to cancer cells, the mitochondrion-specificity of AIEgen-based nanoparticles could further enhance their PDT effects. Liu et al. have introduced mitochondrion-specific triphenylphosphine (TPP) and folic acid (FA) into the PEG-encapsulated AIE-active DPBA-TPE (**33**, Fig. 14D) to design FA-**33**-TPP dots with folate-receptor (FR) positive-cell and mitochondrial dual-targeting capabilities for dual-targeting image-guided PDT of cancer cells (Fig. 14E) [120]. Because of FA and TPP on the nanoparticle surface, FA-**33**-TPP dots were selectively internalized into FR positive MCF-7 cells over FR-negative NIH-3T3 cells and subsequently accumulated in mitochondria, showing the characteristic mitochondrial morphology with bright red emission as shown in Fig. 14F. When MCF-7 and NIH-3T3 cells incubated with FA-**31**-TPP dots were irradiated under white light, only MCF-7 cells were gradually induced to dead with increase of the concentration of FA-**33**-TPP dots (Fig. 14G). Moreover, the enhanced anticancer effect for MCF-7 cells based on FA-**33**-TPP dots is attributed to the fact that dual-targeted capability improves the PDT effect on cell apoptosis and death.

Apart from small organic AIEgens, AIE-featured conjugated polymers (CPs) have also been developed for biomedical application [121]. Most CPs possess short-wavelength emission, limiting the application *in vivo*, especially image-guided PDT. Ideally, photosensitizers should emit at far-red or near-infrared (FR/NIR) region (650–900 nm) and sufficiently generate ROS to kill cancer cells under light irradiation [110]. Thus, design of AIE-active FR/NIR CPs with effective ROS generation not only prompt the development of image-guided PDT but also improve the processability of materials.

Liu et al. have firstly integrated electron-donating TPE and electron-withdrawing AQ to design a new AIE-active FR/NIR CP, named PTPEAQ (**34**, Fig. 15A) [122]. Encapsulation of **34** in DSPE-PEG matrix generated nanoparticles with bright far-red emission and excellent ROS generation yield of 82%. Then bioconjugation with targeting groups will drive the nanoparticles to specific cancer cells for image-guided PDT. As shown in Fig. 15B, **34**-NP-HER2 modified with anti-HER2 affibody exhibited specific targeting for HER2-overexpressed SKBR-3 cancer cells with intense red fluorescence. In contrast, **34**-NP-HER2 is more photostable than commercial photosensitizer Rose Rangal (RB) besides the higher ROS quantum yield, fully suggesting that **34**-NP-HER2 can act as a better photosensitizer for therapy. MTT assays also clearly indicated the selective PDT treatment on SKBR-3 cancer cells over NIH-3T3 normal cells (Fig. 15C). Notably, **34**-NP-HER2 is the first CP for image-guided PDT, which could largely inspire more AIE-active CPs be developed for clinical practice.

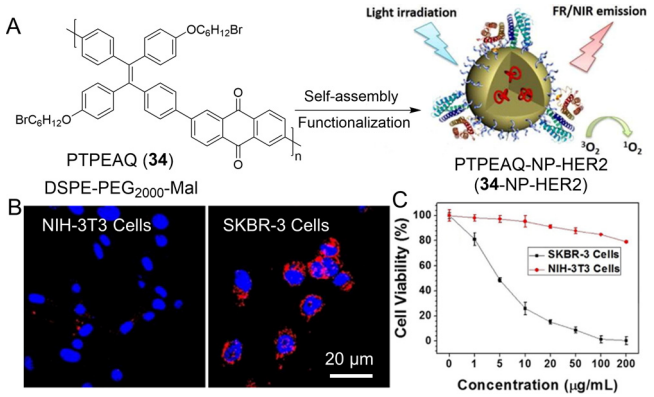

Fig. 15. (A) Schematic illustration of fabrication of PTPEAQ-NP-HER2 (**34**-NP-HER2). (B) Confocal images of NIH-3T3 cells or SKBR-3 cancer cells after incubation of the cells with **34**-NP-HER2 (10 μg mL^{-1}) for 2 h. The red fluorescence of **34**-NP-HER2 was collected above 560 nm upon excitation at 488 nm, and the blue fluorescence of Hoechst was collected between 430 and 470 nm upon excitation at 405 nm. (C) Cell viabilities of **34**-NP-HER2 treated NIH-3T3 and SKBR-3 cells under light irradiation (60 mW cm^{-2}, 5 min). Image is taken from Ref. [122] with permission. (For interpretation of the references to colour in this figure legend, the reader is referred to the web version of this article.)

Recent researches suggest the high level of vascular endothelial growth factor (VEGF) upregulated by angiogenesis can resist cellular ageing and reduce the PDT efficacy for tumor treatment [123]. It is reported that small interfering RNA-VEGF (siVEGF) can suppress the VEGF expression [124], thus designing AIEgen-based nanoparticles with siRNA delivery capability could offer a synergistic effect to enhance image-guided PDT efficacy. Liu and our group encapsulated a ROS-active AIEgen TTD (**35**, Fig. 16A) with siVEGF-modified DSPE-PEG polymer and cRGD peptide to afford cRGD-siVEGF-**35** NPs [125]. The cRGD peptide selectively targeting to integrin facilitates the high internalization efficiency of cRGD-siVEGF-**35** NPs to integrin-overexpressed cells. As shown in Fig. 16B, intense red emission from cRGD-siVEGF-**35** NPs was clearly observed in integrin-overexpressed MDAMB-231 cells. MCF-7 and SK-BR-3 cells without the high expression of integrin showed negligible fluorescence. Moreover, siVEGF in cRGD-siVEGF-**35** NPs exerts an inhibitory effect on the VEGF protein and mRNA expression. Fig. 16C suggests that the levels of VEGF protein and mRNA expression in MDA-MB-231 cells were effectively reduced by 50% and 64% with treatment of cRGD-siVEGF-**35** NPs, respectively. As a consequence, the resistance to PDT for cRGD-siVEGF-**35** NPs was largely attenuated. Without light irradiation, about 61% of MDA-MB-231 cells were killed through RNA interference caused by released siVEGF from cRGD-siVEGF-**35** NPs after 48 h. Further decrease in the cell viability of MDA-MB-231 cells to 25% was resulted under light illumination (Fig. 16C). For other cells such as SK-BR-3 and MCF-7, there is no therapy effect due to no internalization of cRGD-siVEGF-**35** NPs. This example demonstrated the synergistic effect of RNA interference and PDT effect integrated in multifunctional theranostic systems for more effective therapeutic efficacy.

Real-time reporting of the therapeutic efficacy *in situ* undoubtedly provides vital information for precise cancer treatment [126]. Fluorophores with capability of multicolor emission excited by one single wavelength are highly desirable for real-time monitoring of multiple processes. Latest development has demonstrated that monitoring of multiple processes based on one molecular probe could be well performed based on AIEgens [127–132], and the activatable PDT effect together with prediction of therapeutic response *in situ* could be reported simultaneously. AIE-active TPETP-SS-DEVD-TPS-cRGD (**36**, Fig. 17A) has been reported by Liu et al. to exhibit good performance in targeted imaging, activatable PDT and real-time self-reporting of therapeutic responses [133]. All processes involved could be monitored by red-emissive TPETP and green-emissive TPS upon excitation of a single-wavelength 405 nm. As illustrated in Fig. 17B, cRGD-decorated **36** selectively targeted to $\alpha_v\beta_3$ integrin-overexpressed cancer cells such as MDA-MB-231. When **36** was internalized by MDA-MB-23 breast cancer cells, the S-S bond in **36** could be cleaved by intracellular reductant GSH to turn on the red fluorescence of released TPETP (Fig. 17C). Subsequently, the TPETP exerted the PDT effect under light irradiation and the generated ROS induced the cell apoptosis. The activated caspase-3/-7 in the apoptotic cell cleaved the DEVD substrate in **36**, resulting strong green fluorescence from the hydrophobic TPS residue (Fig. 17D). Meanwhile, the fluorescence intensity of fluorogenic peptide substrate R110 upon different light irradiation time correlated well with the apoptosis induced TPS residue fluorescence change (Fig. 17E). Further development of new self-reporting AIEgen-based theranostic agents through molecular engineering with longer-wavelength excitation and emission for direct *in vivo* application is promising in personalized medicine.

So far, the reported AIEgen-based photosensitizers have mainly been utilized for PDT with the goal of causing the death of cancer cells and bacteria. The ROS generation efficiency of this kind of

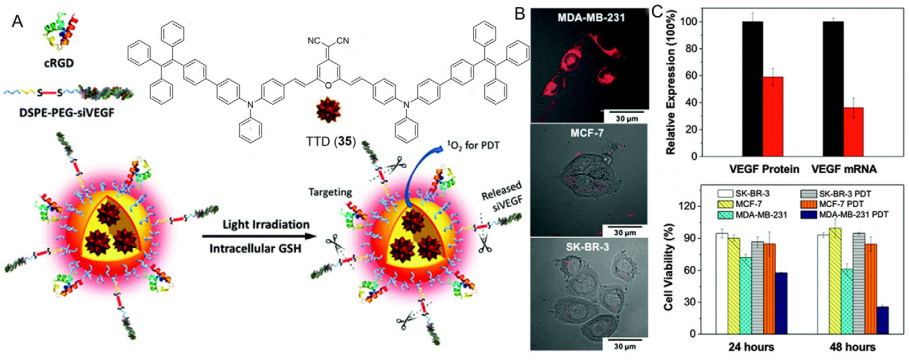

Fig. 16. (A) Structure of AIEgen TTD (**35**) and schematic illustration of cRGD-siVEGF-**35** NPs in the response of intracellular GSH. (B) Confocal images of MDA-MB-231, MCF-7 and SK-BR-3 cells after incubation with cRGD-siVEGF-**35** NPs (5 μg mL^{-1} of **35**) for 4 h at 37 °C. The red fluorescence was from cRGD-siVEGF-**35** NPs (Ex: 488 nm). (C) (Up) The relative VEGF protein expressed in cRGDsiVEGF-**35** NPs (5 μg mL^{-1} of **35**) treated MDA-MB-231 cells and the VEGF mRNA level determined from the lysate of MDA-MB-231 cells (red). Controls were shown in black and set to be 100%. (Down) Viabilities of MDA-MB-231, MCF-7 and SK-BR-3 cells after incubation with cRGD-siVEGF-**35** NPs (5 μg mL^{-1} of **35**) for 4 h followed by light irradiation (0.20 W cm^{-2}, 10 min) and further incubation in fresh medium for 24 and 48 h. Images are taken from Ref. [125] with permission. (For interpretation of the references to colour in this figure legend, the reader is referred to the web version of this article.)

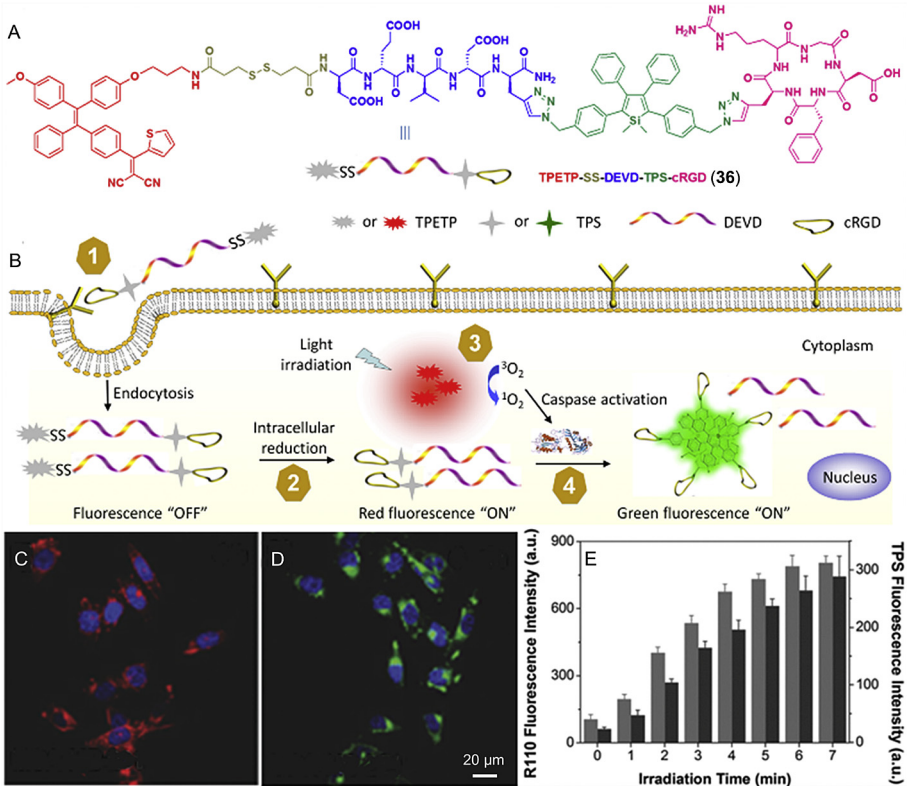

Fig. 17. (A) Structure of TPETP-SS-DEVD-TPS-cRGD (**36**). (B) Schematic illustration of the dual-targeted probe for real-time and *in situ* monitoring of photosensitizer activation and the therapeutic responses. (C and D) Confocal images of MDA-MB-231 cells after incubation with **36** for 4 h with light irradiation of 0 (C) and 6 (D) min. Cell nuclei stained with Hoechst shows blue emission (Ex: 405 nm; Em: 430–470 nm); red fluorescence from the TPETP residue (Ex: 405 nm; Em: > 560 nm); green fluorescence from TPS residue (Ex: 405 nm; Em: 505–525 nm). (E) Cytotoxicity monitored using CytoTox-Fluor cytotoxicity assay and TPS residue fluorescence intensity change of MDA-MB-231 cells upon treatment with **36** (10 μM) for 4 h with different irradiation time. Images are taken from Ref. [133] with permission. (For interpretation of the references to colour in this figure legend, the reader is referred to the web version of this article.)

photosensitizers is highly desirable for therapy. Alternatively, the photosensitizers with low ROS production may also provide new opportunities as a nontoxic "adjuvant" to amplify the antitumor efficacy of chemo-drugs and radiotherapy [134]. With this concept, a theranostic system based on AIEgens integrated diagnosis and chemo-/radiotherapy adjuvant function is desirable to develop for the development of personalized treatment. Recently, Ding and our group have designed novel AIEgen-based photosensitizers as adjuvants for enhancing the therapeutic effect of chemotherapy and radiotherapy [135,136], performing better than widely used agents, which largely extends the application scope of AIE-based photosensitizers.

Ding et al. has developed AIE-active adjuvant TPE-Py-FFGYSA (**37**, Fig. 18A) [135]. The peptide sequence YSA can selectively target EphA2 protein which is overexpressed in many types of cancer such as PC-3. The tripeptide FFG acted as a self-assembly-aided unit to induce the aggregation of **37**. As shown in Fig. 18B, **37** can selectively internalize into PC-3 cells and aggregated to induce the intense yellow-emissive in PC-3 cells, while negligible emission was detected in EphA2-negative smooth muscle cells. On the other hand, **37** can act as a medium photosensitizer to generate certain of ROS, which provides an intracellular oxidative environment but without killing the cancer cells. Fig. 18C revealed the almost no cytotoxicity for PC-3 and smooth muscle cells after treatments by **37** with and without light irradiation. When **37**-treated PC-3 cells were incubated with Ptx, the antitumor efficacy of Ptx was dramatically amplified only under the treatment of both **37** and light irradiation (Fig. 18D), indicating the adjuvant role of **37** in promoting the therapeutic effects of Ptx. Western blot studies in Fig. 18E further revealed that such synergistic antitumor efficacy is originated in the enhanced inhibition of *p*-Akt, leading to a more effective inducement of mitochondria-originated apoptosis. This strategy shows the synergistic effect of "0 + 1>1", which brings a new insight for drug development based on AIEgens.

Radiotherapy is usually utilized as a first line therapy for cancers [137]. Radiosensitizers could make cancer cells more sensitive to radiotherapy. Previous studies have demonstrated the key role of mitochondrion in determining radiation sensitivity of cancer cells for the oxidative stress occurred in mitochondria can result in mitochondrial permeability transition [7]. Inspired by these, Ding and our group designed an AIE-characterized DPA-SCP (**38**, Fig. 19A) [136] with the features of specific mitochondrial targeting and moderate light induced $^1O_2$ generation. As Fig. 19B suggested, A549 lung carcinoma cells stained with **38** emitted strong red fluorescence, exhibiting high mitochondrion-specificity. Notably, the photosensitizer feature of **38** under white light irradiation just offer an increased $^1O_2$ environment in the mitochondria without inducing the death of cancer cells, and then such oxidative environment greatly enhanced the radiosensitivity of cancer cells to ionizing radiation (Fig. 19C). Clonogenic survival assays in Fig. 19D depicted the enhanced radiotherapy effect on A549 cancer cells significantly sensitized by **38** and light irradiation together, and the radiosensitization effect of **38** was larger than the currently available radiosensitizers AuNPs and paclitaxel. Noteworthy, the SER10 value of the combination of "**38** + light irradiation" gave an ultra-high SER10 value of 1.62 for lung cancer cells, much higher than that of AuNPs and paclitaxel with SER10 of 1.19 and 1.32,

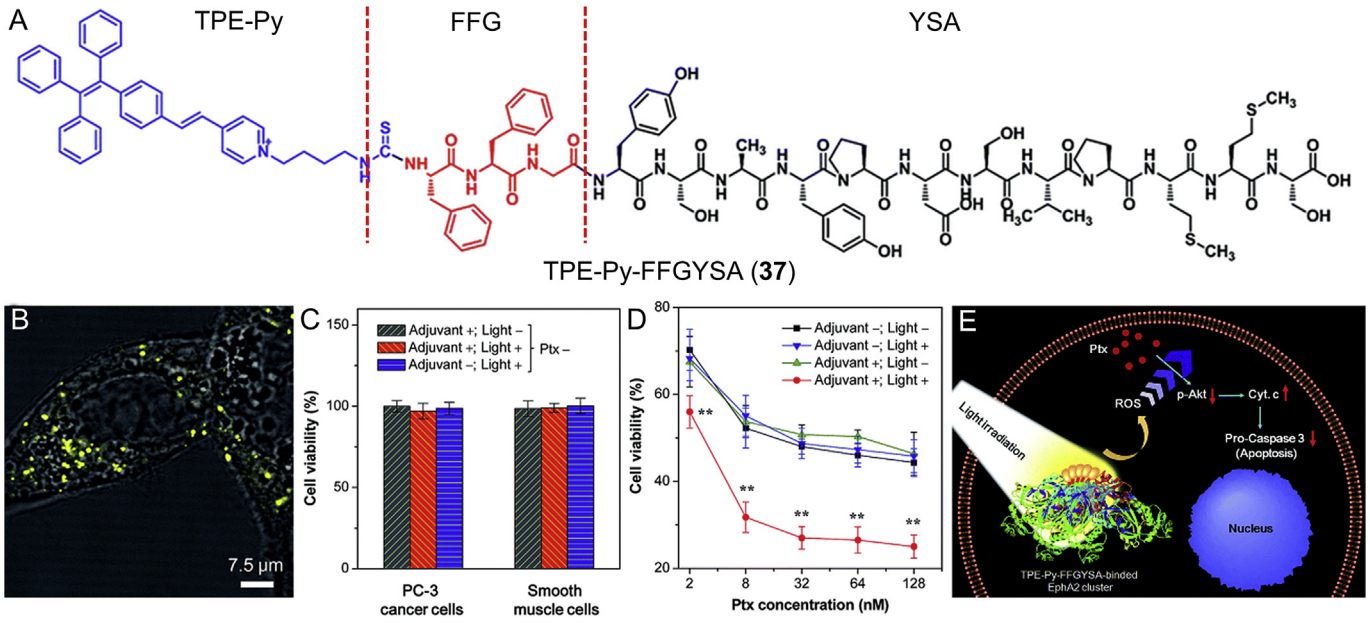

Fig. 18. (A) Structure of EphA2-targeting TPE-Py-FFGYSA (Adjuvant **37**). (B) Confocal images of PC-3 cells after incubation with **37** (1 μM) at 0 °C for 1 h, followed by incubation at 37 °C for another 60 min. (C) Cell viabilities of PC-3 and smooth muscle cells upon different treatments of **37** and light irradiation for 48 h. (D) Cell viabilities of PC-3 cells after addition of various concentrations of Ptx for 48 h. PC-3 cells were treated differently by **37** and light irradiation. For (C) and (D), light irradiation was performed three times at 12, 24, and 36 h after addition of Ptx (no Ptx was added for (C)). ** in (D) represents $P < 0.01$ versus the Ptx alone group (adjuvant -; light-). (E) Proposed synergistic mechanism: the elevated intracellular ROS level resulting from "Adjuvant +; Light +" implies the action of Ptx by enhancing the inhibition of *p*-Akt. Images are taken from Ref. [135] with permission.

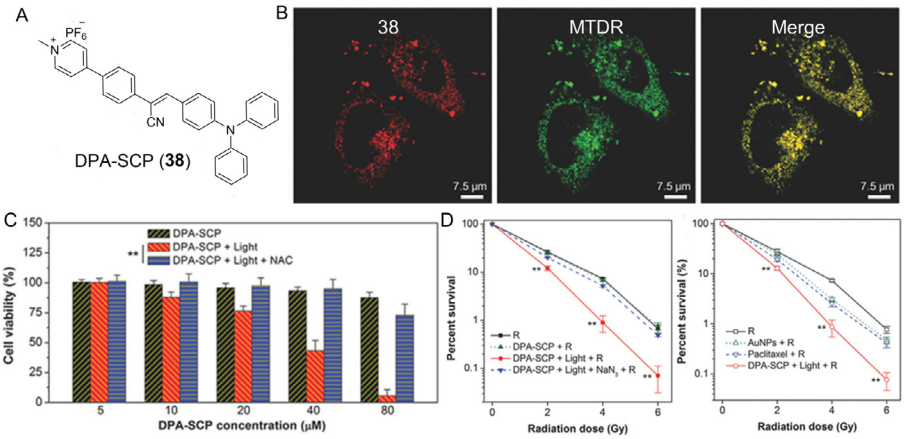

Fig. 19. (A) Structure of AIEgen DPA-SCP (**38**). (B) Confocal images indicate the co-localization of **38** (5 μM) with commercial mitochondrion-staining agent MitoTracker Deep Red FM (MTDR) in A549 cancer cells. (C) Cell viabilities of different treatments with a series of doses of **38** against A549 cancer cells by XTT assay. **represents $P < 0.01$, in comparison between the groups with and without addition of NAC. (D) Survival curves of A549 cancer cells upon various treatments. **represents $P < 0.01$ versus other three treatment groups at each radiation dose. And survival curves of A549 cancer cells pretreated with different radiosensitizers. ** represents $P < 0.01$ versus either the group of "AuNPs + R" or "Paclitaxel + R". Images are taken from Ref. [136] with permission. (For interpretation of the references to colour in this figure legend, the reader is referred to the web version of this article.)

respectively. This work brings new insights into radiotherapy, and provides a promising potential of further exploration of the AIEgen-based photosensitizers with excitation and emission in NIR region as radiosensitizers for radiotherapy *in vivo*.

Abovementioned image-guided chemotherapy and PDT have their own therapeutic mechanisms and unique effects. The combination of chemotherapy and PDT in one system will promisingly give a more effective and integrated therapeutic efficiency with minimized side effects. Besides, combinational therapy of chemotherapy and PDT could also provide a promising alternative to eliminate the disadvantages of chemotherapy alone. Consequently, two kinds of design strategies have been developed for image-guided chemo-photodynamic combination therapy and achieved better therapeutic efficiency than chemotherapy or PDT only [138–140].

One strategy is the conjugation of chemical drugs and AIE-active photosensitizers together. Our group has reported TPECB-Pt-D5-cRGD (**39**, Fig. 20A) with platinum(IV) prodrug (Pt) and ROS-efficient TPECB [138]. Fig. 20B depicted the rationale of the real-time monitoring of drug activation *in situ* as well as the combinatorial photodynamic-chemotherapy against cisplatin resistant cancer cells. Because of cRGD, **39** can be internalized by $\alpha_v\beta_3$ integrin overexpressed cancer cells such as MDA-MB-231 and U87-MG, and then **39** can be activated by GSH inducing the red

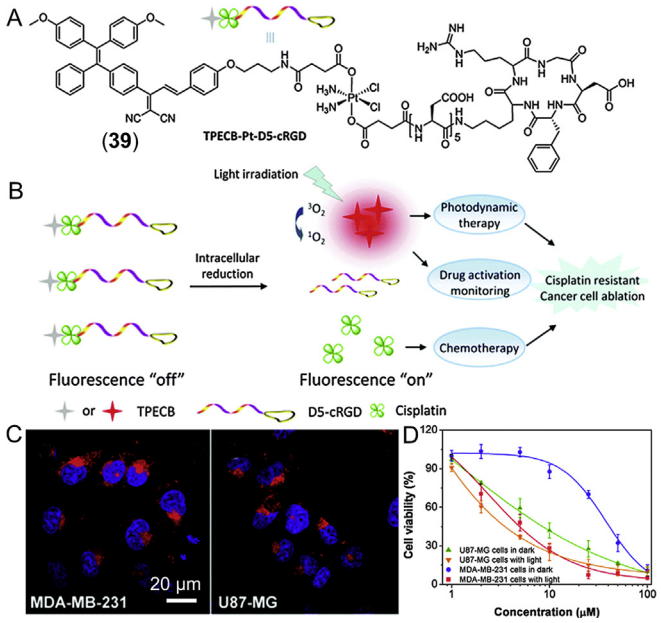

Fig. 20. (A) Structure of TPECB-Pt-D5-cRGD (**39**). (B) Schematic illustration of **39** for image-guided combinatorial PDT and chemotherapy for cisplatin resistant cancer cells. (C) Confocal images of MDA-MB-231 and U87-MG cells upon incubation with **39** for different time. The red fluorescence is from TPECB (Ex: 405 nm; Em: > 560 nm); the blue fluorescence is from cell nuclei stained with Hoechst (Ex: 405 nm; Em: 430–470 nm). (D) Viabilities of U87-MG and MDA-MB-231 cells upon incubation with **39** under dark conditions or light irradiation (1 min, 0.25 W cm^{-2}) and further incubation for 72 h in a fresh medium. Images are taken from Ref. [138] with permission. (For interpretation of the references to colour in this figure legend, the reader is referred to the web version of this article.)

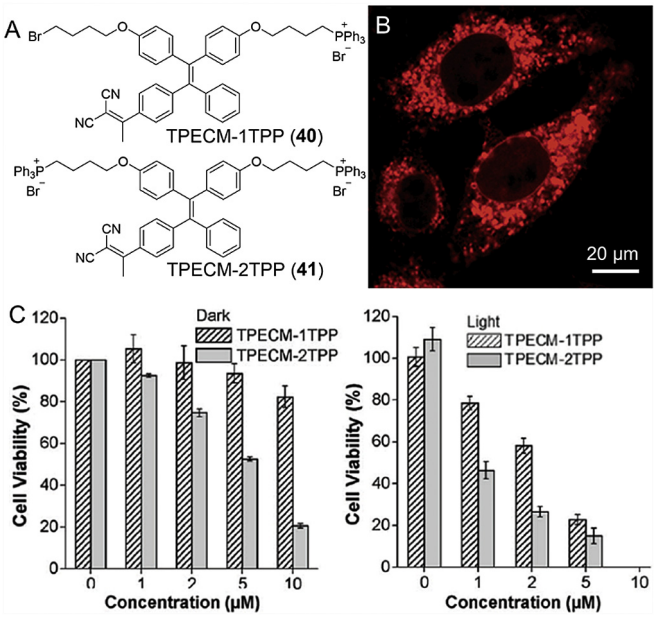

Fig. 21. (A) Structures of TPECM-1TPP (**40**) and TPECM-2TPP (**41**). (B) Confocal images of HeLa cells after incubation with **41** (2 μM), indicating the specificity of **41** to mitochondria of HeLa. (C) Viabilities of HeLa cells after addition of various concentrations of **40** and **41** under dark and white light irradiation. Images are taken from Ref. [139] with permission.

emission of AIE-active TPECB moiety (Fig. 20C). Due to the drug effect of cisplatin part in **39**, the cell viabilities of cisplatin-sensitive U87-MG cells stained with **39** under dark and light irradiation are similar, while the cytotoxicity of **39** to cisplatin-resistant MDA-MB-231 cells enhanced remarkably upon light irradiation compared to that under dark (Fig. 20D). These results clearly demonstrate that the anti-proliferative effect of **39** against cisplatin-resistant MDA-MB-231 cancer cells has been greatly enhanced by the synergistic effect of both chemotherapy and photodynamic therapy.

The other strategy is to develop multifunctional AIEgens integrated with imaging, chemotherapy and PDT together. Previous studies demonstrated that the damage of mitochondria is evidently considered as the main reason for cell apoptosis [112]. Thus, mitochondrion can be selected as the ideal organelle for combined chemotherapy and PDT. Design of bright emissive, ROS-efficient and mitochondrion-specific AIEgens largely offers the unique opportunity for image-guided combination of chemotherapy and PDT.

Liu et al. have developed TPECM-1TPP (**40**) and TPECM-2TPP (**41**) with high mitochondria targeting ability (Fig. 21A) [126]. As shown in Fig. 21B, **40** and **41** specifically accumulated in mitochondria of HeLa cells to turn on their red emission. MTT assays of **40** and **41** under dark indicated that **40** exhibited low cytotoxicity while **41** was much higher dark cytotoxicity to HeLa cells (Fig. 21C). This may be attributed to the fact that **41** selectively exert potent chemo-cytotoxicity on cancer cells by depolarization of MMP. Further, **41** can efficiently generate ROS with strong photo-toxicity upon light illumination, which largely enhances the anti-cancer effect. Thus **41** represents a new generation of subcellular targeted theranostic agent with multifunction, such as cancer cell detection, imaging, chemotherapy, and photodynamic therapy.

5. Conclusion and perspective

Since the AIE concept was firstly promoted by Tang in 2001 [27], AIE research has been advancing rapidly in the areas of optoelectronics, chemo-/biosensors, bioimaging, diagnosis and therapy [28,141,142]. AIEgens have emerged as a class of novel functional materials that emit more brilliantly in the aggregated state than in the solution state, in a sharp contrast to conventional ACQ luminophores. Because of their advantages of superior resistance to photobleaching, large Stokes shift, high signal-to-noise ratio and anti-ACQ effect, AIEgens have been widely applied in biomedical research and their clinical practical applications have been widely explored. In this review, we have introduced the AIE phenomenon and summarized the recent research work in applications of AIEgens in monitoring of biological processes as well as diagnosis and therapy of diseases.

Monitoring of essential biological processes is of great significance for deep insights into the nature of life. To achieve the monitoring in real-time, distinct and long-term fashion, it desires fluorophores with large photostability and high brightness. Traditional fluorophores with ACQ effect hardly satisfy these demands possibly due to the low working concentration leading to easy photobleaching. AIEgens with the targeting ability to subcellular structures such as lysosome, mitochondrion, nucleic acids and phosphatidylserine-based membrane as well as substrates of apoptosis-related enzymes have been developed for real-time monitoring the biological events, for example autophagy, mitophagy, mitochondrial membrane changes and dynamics, cell mitosis, and long-term stem cell tracing as well as cell apoptosis, exhibiting the excellent resistance to photobleaching and high image contrast. These representative examples suggest that AIEgens could act as ideal materials for monitoring of various biological processes at molecular, cellular and tissue levels.

AIEgens can also perform well in diagnosis of diseases. AIEgens with inherent positive charges realized the differentiation of cancer cells over normal cells, based on the difference in mitochondrial

membrane potential between cancer and normal cells. AIEgen-based nanoparticles usually utilized the merits of strong emission in aggregate. The shape-dependent tumor targeting capabilities of AIEgen nanoparticles have been studied and indicated that sphere-shaped nanoparticles are preferential to accumulate in tumors by enhanced permeability and retention effect, thus enable them to distinguish tumors against normal tissues. With the modification of different targeting groups such as various antibodies, streptavidin, cRGD, folic acid and Tat peptide, polymer-encapsulated AIEgen-based nanoparticles were endowed the ability to recognize different types of cancer cells for diagnosis. Apart from the diagnosis of diseases, incorporation of ROS-responsive AIEgens into nanoparticles can realize the diagnosis of inflammation. Precisely size-controlled AIEgen-based nanoparticles can be used to evaluate the BBB damage with better performance than clinically used EB. In addition, dual-modal fluorescent-MRI contrast agents combining AIE property and magnetic relaxivity have been designed for clinical diagnosis.

AIEgens are not only used for diagnosis of diseases but also act as theranostic agents showing their great potential in theranostics, especially for cancers. As part of AIEgens bearing the functionalities of chemotherapy, photodynamic therapy (PDT) or radiotherapy accompanied with imaging, it will enable theranostic systems for image-guided chemotherapy, PDT, radiotherapy and so on. AIEgen-modified traditional cancer drugs will reveal the pharmacodynamics of drugs and evaluate the therapeutic efficacy by imaging. For AIEgens in the form of aggregates or PEG-encapsulated nanoparticles possess the capability of PDT, image-guided PDT systems have been developed to treat various cancers. Due to the short lifetime of ROS, mitochondrion-specific AIEgen-based photosensitizers will largely enhance the therapeutic performance of PDT for accurate therapy. AIEgens and AIE polymers with different targeting groups specifically enter into the corresponding cancer cells will facilitate the treatment effectiveness of image-guided PDT. Insider cells, VEGF will attenuate the therapeutic effect of PDT by inducing angiogenesis. siVEGF was co-encapsulated into AIE nanoparticles to suppress the expression of VEGF to enhance the effect of PDT. Enzyme-responsive activatable AIEgen-based PSs were designed to *in situ* report the therapeutic effects during the treatment. On the other hand, AIEgens with low ROS generation efficiency were also used as adjuvants to increase the therapeutic efficacy of chemo-drugs and as radiosensitizers for the enhancement of radiotherapy effects. Further, the combination of image-guided chemotherapy and PDT that integrated the imaging, chemotherapy and PDT abilities into one AIEgen molecule realize the multifunctional theranostic system with superior therapeutic effects.

Thus, AIEgens have superiority in the application of monitoring of biological processes and diagnosis and therapy of diseases, which will enable them wider applications in pathogenesis, drug development and evaluation, clinic diagnosis and therapy. However, AIEgens still face some challenges for clinical/*in vivo* applications, such as the large penetration depth, the excellent targeting ability, the high ROS generation efficiency, the superior biocompatibility and safety, and so forth. Thus, future development of AIEgens for biological monitoring and theranostics could be advanced from increasing penetration depth of tissues, minimizing interference of biosubstrates, increasing the sensitivity and specificity of biosamples, evaluating the biocompatibility and safety *in vivo* and developing high-efficient theranostic agents for diseases. Photoacoustic (PA) imaging technique is emerging due to its superior penetration depth of millimeter to centimeter [143], AIEgens with many rotors theoretically possess good PA property and that will bring great potential for PA imaging for *in vivo* application. Meanwhile, the small-region heat generated by AIE-active PA probes could further provide the photothermal therapy (PTT) for tumor. On the other hand, development of AIEgens with long-wavelength excitation and emission such as NIR and two-photon excitable emission could also penetrate relatively deeply into tissues with less photodamage to biosubstrates and less autofluorescence, which could greatly facilitate *in vivo* imaging and monitoring of biological processes. If integrated with other functionalities such as radiotherapy, chemotherapy and phototherapy, it will potentially offer the opportunity of traceable cancer therapy for personalized medicine, and guide the surgeons in the real-time visualization cell ablation and removal of tumors with a high tumor-to-normal tissue ratio. Apart from fluorescence, another approach to reduce interference of biosubstrates is developing phosphorescent probes, because phosphorescence materials could naturally avoid the autofluorescence of biosubstrates [144]. AIEgens with room-temperature phosphorescence (RTP) develop rapidly and should potentially prompt the imaging and monitoring of biological processes and diagnosis of diseases in the manner of extremely low interference. For theranostics, previous work has demonstrated that AIEgens accumulated in lysosomes could affect the functionality of autophagy, bringing the death of cancer cells to realize the therapy as drugs [109]. Mitochondrion-specific AIE probes with inherent positive charges would selectively accumulate in mitochondria of cancer cells due to their higher MMP [85]. The excess amount of AIE probes accumulated in mitochondria will seriously disrupt the normal physiological functionalities, inducing the death of cancer cells to achieve the aim of therapy. Therefore, AIEgens with inherent subcellular targeting will trend to excessively accumulate in subcellular organelles, which would seriously disturb the normal metabolism inducing the apoptosis-induced ablation, potentially endowing them as effective theranostic drugs for biomedicine. In addition, some important issues such as biocompatibility, biosafety, biodistribution and metabolism of AIEgens are exigent to be clarified, which will profoundly promote the further clinical applications of AIEgens. At this time, more and more outstanding results on biomedical applications of AIEgens have been reported, depicting the rapid development of AIE. We enthusiastically look forward to new developments in this exciting area of research.

Acknowledgement

This work was partially supported by the Innovation and Technology Commission (ITC-CNERC14SC01), the National Basic Research Program of China (973 Program; 2013CB834701 and 2013CB834702), the University Grants Committee of Hong Kong (AoE/P-03/08), the Research Grants Council of Hong Kong (16305015, 16308016, C2014-15G, N-HKUST604/14 and AHKUST605/16). B. Z. T. is also grateful for the support from the Guangdong Innovative Research Team Program of China (201101C0105067115), the Science and Technology Plan of Shenzhen (JCYJ20160229205601482) and the Shenzhen Peacock Plan.

References

[1] M. Mossio, M. Montévil, G. Longo, Theoretical principles for biology: Organization, Prog. Biophys. Mol. Bio. 122 (2016) 24–35.
[2] S.C.L. Kamerlin, A. Warshel, At the dawn of the 21st century: is dynamics the missing link forunderstanding enzyme catalysis? Proteins Struct. Funct. Bioinforma. 78 (2010) 1339–1375.
[3] K. Moldave, Nucleic acids and protein biosynthesis, Annu. Rev. Biochem. 34 (1965) 419–448.
[4] N. Mizushima, M. Komatsu, Autophagy: renovation of cells and tissues, Cell 147 (2011) 728–741.
[5] A.I. Lamond, C.E. William, Structure and function in the nucleus, Science 280 (1998) 547–553.

[6] M.C.S. Lee, E.A. Miller, J. Goldberg, L. Orci, R. Schekman, Bi-directional protein transport between the ER and Golgi, Annu. Rev. Cell Dev. Biol. 20 (2004) 87–123.
[7] D.C. Chan, Mitochondria: dynamic organelles in disease, aging, and development, Cell 125 (2006) 1241–1252.
[8] Z.J. Liu, Y. Zhuge, O.C. Velazquez, Trafficking and differentiation of mesenchymal stem cells, J. Cell. Biochem. 106 (2009) 984–991.
[9] M.O. Hengartner, The biochemistry of apoptosis, Nature 407 (2000) 770–776.
[10] D. Hanahan1, R.A. Weinberg, The hallmarks of cancer, Cell 100 (2000) 57–70.
[11] J. Hardy, D.J. Selkoe, The amyloid hypothesis of alzheimer's disease: progress and problems on the road to therapeutics, Science 297 (2002) 353–356.
[12] D.M. Nathan, Long-term complications of diabetes mellitus, New Engl. J. Med. 328 (1993) 1676–1685.
[13] K. Tánaka, High resolution scanning electron microscopy of the cell, Biol. Cell 65 (1989) 89–98.
[14] M. Eltsov, B. Zuber, Transmission electron microscopy of the bacterial nucleoid, J. Struct. Biol. 156 (2006) 246–254.
[15] S.S. Gambhir, Molecular imaging of cancer with positron emission tomography, Nat. Rev. Cancer 2 (2002) 683–693.
[16] D.J. Brenner, E.J. Hall, Computed tomography-an increasing source of radiation exposure, New Engl. J. Med. 357 (2007) 2277–2284.
[17] M.D. Fox, M.E. Raichle, Spontaneous fluctuations in brain activity observed with functional magnetic resonance imaging, Nat. Rev. Neurosci. 8 (2007) 700–711.
[18] J.E. Kennedy, High-intensity focused ultrasound in the treatment of solid tumours, Nat. Rev. Cancer 5 (2005) 321–327.
[19] W.R. Zipfel, R.M. Williams, W.W. Webb, Nonlinear magic: multiphoton microscopy in the biosciences, Nat. Biotechnol. 21 (2003) 1369–1377.
[20] J.W. Lichtman, J.A. Conchello, Fluorescence microscopy, Nat. Meth. 2 (2005) 910–919.
[21] B. Huang, M. Bates, X. Zhuang, Super-resolution fluorescence microscopy, Annu. Rev. Biochem. 78 (2009) 993–1016.
[22] P.I.H. Bastiaens, A. Squire, Fluorescence lifetime imaging microscopy: spatial resolution of biochemical processes in the cell, Trends Cell Biol. 9 (1999) 48–52.
[23] N.C. Shaner, G.H. Patterson, M.W. Davidson, Advances in fluorescent protein technology, J. Cell Sci. 120 (2007) 4247–4260.
[24] X. Michalet, F.F. Pinaud, L.A. Bentolila, J.M. Tsay, S. Doose, J.J. Li, et al., Quantum dots for live cells, in vivo imaging, and diagnostics, Science 307 (2005) 538–544.
[25] Y. Su, M. Hu, C. Fan, Y. He, Q. Li, W. Li, et al., The cytotoxicity of CdTe quantum dots and the relative contributions from released cadmium ions and nanoparticle properties, Biomaterials 31 (2010) 4829–4834.
[26] J. Mei, Y. Hong, J.W.Y. Lam, A. Qin, Y. Tang, B.Z. Tang, Aggregation-induced emission: the whole is more brilliant than the parts, Adv. Mater. 26 (2014) 5429–5479.
[27] J.D. Luo, Z.L. Xie, J.W.Y. Lam, L. Cheng, H.Y. Chen, C.F. Qiu, et al., Aggregation-induced emission of 1-methyl-1,2,3,4,5-pentaphenylsilole, Chem. Commun. (2001) 1740–1741.
[28] J. Mei, N.L.C. Leung, R.T.K. Kwok, J.W.Y. Lam, B.Z. Tang, Aggregation-induced emission: together we shine, united we soar!, Chem. Rev. 115 (2015) 11718–11940.
[29] M. Kang, X. Gu, R.T.K. Kwok, C.W.T. Leung, J.W.Y. Lam, F. Li, et al., A near-infrared AIEgen for specific imaging of lipid droplets, Chem. Commun. 52 (2016) 5957–5960.
[30] S.S. Kelkar, T.M. Reineke, Theranostics: combining imaging and therapy, Bioconjugate Chem. 22 (2011) 1879–1903.
[31] G. Feng, B. Liu, Multifunctional AIEgens for future theranostics, Small 12 (2016) 6528–6535.
[32] Y. Hong, J.W.Y. Lam, B.Z. Tang, Aggregation-induced emission: phenomenon, mechanism and applications, Chem. Commun. (2009) 4332–4353.
[33] M. Wang, G. Zhang, D. Zhang, D. Zhu, B.Z. Tang, Fluorescent bio/chemosensors based on silole and tetraphenylethene luminogens with aggregation-induced emission feature, J. Mater. Chem. 20 (2010) 1858–1867.
[34] Y. Hong, J.W.Y. Lam, B.Z. Tang, Aggregation-induced emission, Chem. Soc. Rev. 40 (2011) 5361–5388.
[35] D. Ding, K. Li, B. Liu, B.Z. Tang, Bioprobes based on AIE fluorogens, Acc. Chem. Res. 46 (2013) 2441–2453.
[36] J. Liang, B.Z. Tang, B. Liu, Specific light-up bioprobes based on AIEgen conjugates, Chem. Soc. Rev. 44 (2015) 4228–4238.
[37] S. Chen, H. Wang, Y. Hong, B.Z. Tang, Fabrication of fluorescent nanoparticles based on AIE luminogens (AIE dots) and their applications in bioimaging, Mater. Horiz. 3 (2016) 283–293.
[38] B. Liu, Aggregation-induced emission: materials and biomedical applications, MRS Bull. 42 (2017) 458–463.
[39] F. Hu, B. Liu, Organelle-specific bioprobes based on fluorogens with aggregation-induced emission (AIE) characteristics, Org. Biomol. Chem. 14 (2016) 9931–9944.
[40] X. Zhang, K. Wang, M. Liu, X. Zhang, L. Tao, Y. Chen, et al., Polymeric AIE-based nanoprobes for biomedical applications: recent advances and perspectives, Nanoscale 7 (2015) 11486–11508.
[41] Q. Wan, Q. Huang, M. Liu, D. Xu, H. Huang, X. Zhang, et al., Aggregation-induced emission active luminescent polymeric nanoparticles: non-covalent fabrication methodologies and biomedical applications, Appl. Mater. Today 9 (2017) 145–160.
[42] Y. Yuan, W. Wu, S. Xu, B. Liu, A biosensor based on self-clickable AIEgen: a signal amplification strategy for ultrasensitive immunoassays, Chem. Commun. 53 (2017) 5287–5290.
[43] J. Niu, J. Fan, X. Wang, Y. Xiao, X. Xie, X. Jiao, et al., Simultaneous fluorescence and chemiluminescence turned on by aggregation-induced emission for real-time monitoring of endogenous superoxide anion in live cells, Anal. Chem. 89 (2017) 7210–7215.
[44] Y. Yuan, B. Liu, Visualization of drug delivery processes using AIEgens, Chem. Sci. 8 (2017) 2537–2546.
[45] N. Mizushima, M. Komatsu, Autophagy: renovation of cells and tissues, Cell 147 (2011) 728–741.
[46] B. Levine, G. Kroemer, Autophagy in the pathogenesis of disease, Cell 132 (2008) 27–42.
[47] N. Mizushima, Autophagy: process and function, Genes Dev. 21 (2007) 2861–2873.
[48] S.L. Shen, X.P. Chen, X.F. Zhang, J.Y. Miao, B.X. Zhao, A rhodamine B-based lysosomal pH probe, J. Mater. Chem. B 3 (2015) 919–925.
[49] C.W.T. Leung, Z. Wang, E. Zhao, Y. Hong, S. Chen, R.T.K. Kwok, et al., A Lysosome-targeting AIEgen for autophagy visualization, Adv. Healthc. Mater. 5 (2016) 427–431.
[50] A. Heiseke, Y. Aguib, C. Riemer, M. Baier, H.M. Schätzl, Lithium induces clearance of protease resistant prion protein in prion-infected cells by induction of autophagy, J. Neurochem. 109 (2009) 25–34.
[51] R.J. Youle, D.P. Narendra, Mechanisms of mitophagy, Nat. Rev. Mol. Cell Biol. 12 (2011) 9–14.
[52] C.W.T. Leung, Y. Hong, S. Chen, E. Zhao, J.W.Y. Lam, B.Z. Tang, A Photostable AIE luminogen for specific mitochondrial imaging and tracking, J. Am. Chem. Soc. 135 (2013) 62–65.
[53] N. Zhao, S. Chen, Y. Hong, B.Z. Tang, A red emitting mitochondria-targeted AIE probe as an indicator for membrane potential and mouse sperm activity, Chem. Commun. 51 (2015) 13599–13602.
[54] B. Situ, S. Chen, E. Zhao, C.W.T. Leung, Y. Chen, Y. Hong, et al., Real-time imaging of cell behaviors in living organisms by a mitochondria-targeting AIE fluorogen, Adv. Funct. Mater. 26 (2016) 7132–7138.
[55] W. Zhang, R.T.K. Kwok, Y. Chen, S. Chen, E. Zhao, C.Y.Y. Yu, et al., Real-time monitoring of the mitophagy process by a photostable fluorescent mitochondrion-specific bioprobe with AIE characteristics, Chem. Commun. 51 (2015) 9022–9025.
[56] X. Gu, E. Zhao, T. Zhao, M. Kang, C. Gui, J.W.Y. Lam, et al., A mitochondrion-specific photoactivatable fluorescence turn-on AIE-based bioprobe for localization super-resolution microscope, Adv. Mater. 28 (2016) 5064–5071.
[57] C.Y.W. Lo, S. Chen, S.J. Creed, M. Kang, N. Zhao, B.Z. Tang, Novel super-resolution capable mitochondrial probe, MitoRed AIE, enables assessment of real-time molecular mitochondrial dynamics, Sci. Rep. 6 (2016) 30855–30864.
[58] M.Q. Zhu, G.F. Zhang, Z. Hu, M.P. Aldred, C. Li, W.L. Gong, et al., Reversible fluorescence switching of spiropyran-conjugated biodegradable nanoparticles for super-resolution fluorescence imaging, Macromolecules 47 (2014) 1543–1552.
[59] A. Bartelt, J. Heeren, Adipose tissue browning and metabolic health, Nat. Rev. Endocrinol. 10 (2014) 24–36.
[60] M. Gao, C.K. Sim, C.W.T. Leung, Q. Hu, G. Feng, F. Xu, et al., A fluorescent light-up probe with AIE characteristics for specific mitochondrial imaging to identify differentiating brown adipose cells, Chem. Commun. 50 (2014) 8312–8315.
[61] B.A.A. Weaver, D.W. Cleveland, Decoding the links between mitosis, cancer, and chemotherapy: the mitotic checkpoint, adaptation, and cell death, Cancer Cell 8 (2005) 7–12.
[62] D. Rentzeperis, M. Medero, L.A. Marky, Thermodynamic investigation of the association of ethidium, propidium and bis-ethidium to DNA hairpins, Bioorg. Med. Chem. 3 (1995) 751–759.
[63] M. Wang, D. Zhang, G. Zhang, Y. Tang, S. Wang, D. Zhu, Fluorescence turn-on detection of DNA and label-free fluorescence nuclease assay based on the aggregation-induced emission of silole, Anal. Chem. 80 (2008) 6443–6448.
[64] X. Li, K. Ma, S. Zhu, S. Yao, Z. Liu, B. Xu, et al., Fluorescent aptasensor based on aggregation-induced emission probe and graphene oxide, Anal. Chem. 86 (2014) 298–303.
[65] S. Li, S.M. Langenegger, R. Häner, Control of aggregation-induced emission by DNA hybridization, Chem. Commun. 49 (2013) 5835–5837.
[66] J. Huang, M. Wang, Y. Zhou, X. Weng, L. Shuai, X. Zhou, et al., Visual observation of G-quadruplex DNA with the label-free fluorescent probe silole with aggregation-induced emission, Bioorg. Med. Chem. 17 (2009) 7743–7748.
[67] S. Samanta, S. Goswami, Md.N. Hoque, A. Ramesh, G. Das, An aggregation-induced emission (AIE) active probe renders Al(III) sensing and tracking of subsequent interaction with DNA, Chem. Commun. 50 (2014) 11833–11836.
[68] Y. Hong, S. Chen, C.W.T. Leung, J.W.Y. Lam, B.Z. Tang, Water-soluble tetraphenylethene derivatives as fluorescent “Light-Up” probes for nucleic acid detection and their applications in cell imaging, Chem. Asian J. 8 (2013) 1806–1812.
[69] D. Ding, D. Mao, K. Li, X.M. Wang, W. Qin, R.R. Liu, et al., Precise and long-term tracking of adipose-derived stem cells and their regenerative capacity via superb bright and stable organic nanodots, ASC Nano. 8 (2014) 12620–12631.

[70] H. Ma, C. Qi, C. Cheng, Z. Yang, H. Cao, Z. Yang, et al., AIE-active tetraphenylethylene cross-linked N-isopropylacrylamide polymer: a long-term fluorescent cellular tracker, ACS Appl. Mater. Interfaces 8 (2016) 8341–8348.
[71] Z. Wang, S. Chen, J.W.Y. Lam, W. Qin, R.T.K. Kwok, N. Xie, et al., Long-term fluorescent cellular tracing by the aggregates of AIE bioconjugates, J. Am. Chem. Soc. 135 (2013) 8238–8245.
[72] T. Mondal, J. Sarkar, S. Ghosh, Fluorescent PEGulated oligourethane nanoparticles for long-term cellular tracing, Chem. Eur. J. 22 (2016) 10930–10936.
[73] R. Quarto, M. Mastrogiacomo, R. Cancedda, S.M. Kutepov, V. Mukhachev, A. Lavroukov, et al., Repair of large bone defects with the use of autologous bone marrow stromal cells, N. Engl. J. Med. 344 (2001) 385–386.
[74] M. Gao, J. Chen, G. Lin, S. Li, L. Wang, A. Qin, et al., Long-term tracking of the osteogenic differentiation of mouse BMSCs by aggregation-induced emission nanoparticles, ACS Appl. Mater. Interfaces 8 (2016) 17878–17884.
[75] P.R. Walker, J. Leblanc, B. Smith, S. Pandey, M. Sikorska, Detection of DNA fragmentation and endonucleases in apoptosis, Methods 17 (1999) 329–338.
[76] Q.D. Nguyen, G. Smith, M. Glaser, M. Perumal, E. Arstad, E.O. Aboagye, Positron emission tomography imaging of drug-induced tumor apoptosis with a caspase-3/7 specific [18F]-labeled isatin sulfonamide, Proc. Natl. Acad. Sci. U.S.A. 106 (2009) 16375–16380.
[77] R.A. Schlegel, P. Williamson, Phosphatidylserine, a death knell, Cell Death Differ. 8 (2001) 551–563.
[78] B. Plasier, D.R. Lloyd, G.C. Paul, C.R. Thomas, M. Al-Rubeai, Automatic image analysis for quantification of apoptosis in animal cell culture by annexin-V affinity assay, J. Immunol. Methods 229 (1999) 81–95.
[79] J.M. Kwong, C. Hoang, R.T. Dukes, R.W. Yee, B.D. Gray, K.Y. Pak, J. Caprioli, Bis(zinc-dipicolylamine), Zn-DPA, a new marker for apoptosis, Invest. Ophthalmol. Vis. Sci. 55 (2014) 4913–4921.
[80] Q. Hu, M. Gao, G. Feng, X. Chen, B. Liu, A cell apoptosis probe based on fluorogen with aggregation induced emission characteristics, ACS Appl. Mater. Interfaces 7 (2015) 4875–4882.
[81] A.C.S. Leung, E. Zhao, R.T.K. Kwok, J.W.Y. Lam, C.W.T. Leung, H. Deng, B.Z. Tang, An AIE-based bioprobe for differentiating the early and late stages of apoptosis mediated by H_2O_2, J. Mater. Chem. B 4 (2016) 5510–5514.
[82] H. Shi, R.T.K. Kwok, J. Liu, B. Xing, B.Z. Tang, B. Liu, Real-time monitoring of cell apoptosis and drug screening using fluorescent light-up probe with aggregation-induced emission characteristics, J. Am. Chem. Soc. 134 (2012) 17972–17981.
[83] D. Ding, J. Liang, H. Shi, R.T.K. Kwok, M. Gao, G. Feng, et al., Light-up bioprobe with aggregation-induced emission characteristics for real-time apoptosis imaging in target cancer cells, J. Mater. Chem. B 2 (2014) 231–238.
[84] Y. Yuan, C.J. Zhang, R.T.K. Kwok, D. Mao, B.Z. Tang, B. Liu, Light-up probe based on AIEgens: dual signal turn-on for cascade caspase activation monitoring, Chem. Sci. 8 (2017) 2723–2728.
[85] C. Gui, E. Zhao, R.T.K. Kwok, A.C.S. Leung, J.W.Y. Lam, M. Jiang, et al., AIE-active theranostic system: selective staining and killing of cancer cells, Chem. Sci. 8 (2017) 1822–1830.
[86] A. Shao, Y. Xie, S. Zhu, Z. Guo, S. Zhu, J. Guo, Far-red and near-IR AIE-active fluorescent organic nanoprobes with enhanced tumor-targeting efficacy: shape-specific effects, Angew. Chem. Int. Ed. 54 (2015) 7275–7280.
[87] R. Bazak, M. Houri, S. El Achy, S. Kamel, T. Refaat, Cancer active targeting by nanoparticles: a comprehensive review of literature, J. Cancer Res. Clin. Oncol. 141 (2015) 769–784.
[88] M. Das, C. Mohanty, S.K. Sahoo, Ligand-based targeted therapy for cancer tissue, Exp. Opin. Drug Deliv. 6 (2009) 285–304.
[89] M. Gao, H. Su, G. Lin, S. Li, X. Yu, A. Qin, et al., Targeted imaging of EGFR overexpressed cancer cells by brightly fluorescent nanoparticles conjugated with cetuximab, Nanoscale 8 (2016) 15027–15032.
[90] Y. Zhang, K. Chang, B. Xu, J. Chen, L. Yan, S. Ma, et al., Highly efficient near-infrared organic dots based on novel AEE fluorogen for specific cancer cell imaging, Rsc Adv. 5 (2015) 36837–36844.
[91] D. Wang, J. Qian, W. Qin, A. Qin, B.T. Tang, S. He, Biocompatible and photostable AIE dots with red emission for in vivo two-photon bioimaging, Sci. Rep. 4 (2014) 4279–4287.
[92] Y. Jiang, J. Chen, C. Deng, E.J. Suuronen, Z. Zhong, Click hydrogels, microgels and nanogels: emerging platforms for drug delivery and tissue engineering, Biomaterials 35 (2014) 4969–4985.
[93] R. Medzhitov, Origin and physiological roles of inflammation, Nature 454 (2008) 428–435.
[94] Z. Song, D. Mao, S.H.P. Sung, R.T.K. Kwok, J.W.Y. Lam, D. Kong, et al., Activatable fluorescent nanoprobe with aggregation-induced emission characteristics for selective in vivo imaging of elevated peroxynitrite generation, Adv. Mater. 28 (2016) 7249–7256.
[95] G.C.V.D. Bittner, C.R. Bertozzi, C.J. Chang, A strategy for dual-analyte luciferin imaging: *in vivo* bioluminescence detection of hydrogen peroxide and caspase activity in a murine model of acute inflammation, J. Am. Chem. Soc. 135 (2013) 1783–1795.
[96] J.I. Sage, R.L. Van Uitert, T.E. Duffy, Early changes in blood brain barrier permeability to small molecules after transient cerebral ischemia, Stroke 15 (1984) 46–50.
[97] A. Wunder, K. Schoknecht, D.B. Stanimirovic, O. Prager, Y. Chassidim, Imaging blood-brain barrier dysfunction in animal disease models, Epilepsia 53 (2012) 14–21.
[98] X. Cai, A. Bandla, D. Mao, G. Feng, W. Qin, L.D. Liao, et al., Biocompatible red fluorescent organic nanoparticles with tunable size and aggregation-induced emission for evaluation of blood–brain barrier damage, Adv. Mater. 28 (2016) 8760–8765.
[99] L. Frullano, T.J. Meade, Multimodal MRI contrast agents, J. Biol. Inorg. Chem. 12 (2007) 939–949.
[100] Y. Chen, M. Li, Y. Hong, J.W.Y. Lam, Q. Zheng, B.Z. Tang, Dual-modal MRI contrast agent with aggregation-induced emission characteristic for liver specific imaging with long circulation lifetime, ACS Appl. Mater. Interfaces 6 (2014) 10783–10791.
[101] J.M. Idée, S. Louguet, S. Ballet, C. Corot, Theranostics and contrast-agents for medical imaging: a pharmaceutical company viewpoint, Quant. Imaging Med. Surg. 3 (2013) 292–297.
[102] M. Li, Y. Gao, Y. Yuan, Y. Wu, Z. Song, B.Z. Tang, et al., One-step formulation of targeted aggregation-induced emission dots for image-guided photodynamic therapy of cholangiocarcinoma, ACS Nano 11 (2017) 3922–3932.
[103] A. Nicol, W. Qin, R.T.K. Kwok, J.M. Burkhartsmeyer, Z. Zhu, H. Su, et al., Functionalized AIE nanoparticles with efficient deep-red emission, mitochondrial specificity, cancer cell selectivity and multiphoton susceptibility, Chem. Sci. 8 (2017) 4634–4643.
[104] J. Liu, C. Chen, S. Ji, Q. Liu, D. Ding, D. Zhao, et al., Long wavelength excitable near-infrared fluorescent nanoparticles with aggregation-induced emission characteristics for image-guided tumor resection, Chem. Sci. 8 (2017) 2782–2789.
[105] W. Wu, D. Mao, F. Hu, S. Xu, C. Chen, C.J. Zhang, et al., A highly efficient and photostable photosensitizer with near-infrared aggregation-induced emission for image-guided photodynamic anticancer therapy, Adv. Mater. 29 (2017), 1700548, http://dx.doi.org/10.1002/adma.201700548.
[106] B. Gu, W. Wu, G. Xu, G. Feng, F. Yin, P.H.J. Chong, et al., Precise two-photon photodynamic therapy using an efficient photosensitizer with aggregation-induced emission characteristics, Adv. Mater. 29 (2017), 1701076, http://dx.doi.org/10.1002/adma.201701076.
[107] Z. Fan, L. Ren, W. Zhang, D. Li, G. Zhao, J. Yu, AIE luminogen-functionalised mesoporous silica nanoparticles as nanotheranostic agents for imaging guided synergetic chemo-/photothermal therapy, Inorg. Chem. Front. 4 (2017) 833–839.
[108] M. Hilvo, C. Denkert, L. Lehtinen, B. Müller, S. Brockmöller, T. Seppänen-Laakso, Novel theranostic opportunities offered by characterization of altered membrane lipid metabolism in breast cancer progression, Cancer Res. 71 (2011) 3236–3245.
[109] Y. Zhao, R.T.K. Kwok, J.W.Y. Lam, B.Z. Tang, A highly fluorescent AIE-active theranostic agent with anti-tumor activity to specific cancer cells, Nanoscale 8 (2016) 12520–12523.
[110] J.P. Celli, B.Q. Spring, I. Rizvi, C.L. Evans, K.S. Samkoe, S. Verma, Imaging and photodynamic therapy: mechanisms, monitoring, and optimization, Chem. Rev. 110 (2010) 2795–2838.
[111] X. Liang, X. Li, L. Jing, X. Yue, Z. Dai, Theranostic porphyrin dyad nanoparticles for magnetic resonance imaging guided photodynamic therapy, Biomaterials 35 (2014) 6379–6388.
[112] D.R. Green, J.C. Reed, Mitochondria and apoptosis, Science 281 (1998) 1309–1312.
[113] C.C. Chang, M.C. Hsieh, J.C. Lin, T.C. Chang, Selective photodynamic therapy based on aggregation-induced emission enhancement of fluorescent organic nanoparticles, Biomaterials 33 (2012) 897–906.
[114] F. Hu, Y. Huang, G. Zhang, R. Zhao, H. Yang, D. Zhang, Targeted bioimaging and photodynamic therapy of cancer cells with an activatable red fluorescent bioprobe, Anal. Chem. 86 (2014) 7987–7995.
[115] K. Han, S.B. Wang, Q. Lei, J.Y. Zhu, X.Z. Zhang, Ratiometric biosensor for aggregation-induced emission-guided precise photodynamic therapy, ACS Nano 9 (2015) 10268–10277.
[116] Y. Huang, G. Zhang, F. Hu, Y. Jin, R. Zhao, D. Zhang, Emissive nanoparticles from pyridinium-substituted tetraphenylethylene salts: imaging and selective cytotoxicity towards cancer cells in vitro and in vivo by varying counter anions, Chem. Sci. 7 (2016) 7013–7019.
[117] R. Zhang, G. Feng, C.J. Zhang, X. Cai, X. Cheng, B. Liu, Real-time specific light-up sensing of transferrin receptor: image-guided photodynamic ablation of cancer cells through controlled cytomembrane disintegration, Anal. Chem. 88 (2016) 4841–4848.
[118] E. Zhao, H. Deng, S. Chen, Y. Hong, C.W.T. Leung, J.W.Y. Lam, et al., A dual functional AEE fluorogen as a mitochondrial-specific bioprobe and an effective photosensitizer for photodynamic therapy, Chem. Commun. 50 (2014) 14451–14454.
[119] G. Feng, W. Wu, S. Xu, B. Liu, Far red/near-infrared AIE dots for image-guided photodynamic cancer cell ablation, ACS Appl. Mater. Interfaces 8 (2016) 21193–21200.
[120] G. Feng, W. Qin, Q. Hu, B.Z. Tang, B. Liu, Cellular and mitochondrial dual-targeted organic dots with aggregation-induced emission characteristics for image-guided photodynamic therapy, Adv. Healthc. Mater. 4 (2015) 2667–2676.
[121] W. Wu, S. Ye, R. Tang, L. Huang, Q. Li, G. Yu, et al., New tetraphenylethylene-containing conjugated polymers: facile synthesis, aggregation-induced emission enhanced characteristics and application as explosive chemsensors and PLEDs, Polymer 53 (2012) 3163–3171.
[122] W. Wu, G. Feng, S. Xu, B. Liu, A photostable far-red/Near-infrared conjugated polymer photosensitizer with aggregation-induced emission for image-guided cancer cell ablation, Macromolecules 49 (2016) 5017–5025.

[123] D.E. Dolmans, D. Fukumura, R.K. Jain, Photodynamic therapy for cancer, Nat. Rev. Cancer 3 (2003) 380–387.
[124] H.Y. Wang, W.J. Yi, S.Y. Qin, C. Li, R.X. Zhuo, X.Z. Zhang, Tyroserleutide-based gene vector for suppressing VEGF expression in cancer therapy, Biomaterials 33 (2012) 8685–8694.
[125] G. Jin, G. Feng, W. Qin, B.Z. Tang, B. Liu, K. Li, Multifunctional organic nanoparticles with aggregation-induced emission (AIE) characteristics for targeted photodynamic therapy and RNA interference therapy, Chem. Commun. 52 (2016) 2752–2755.
[126] J.M. Gallo, P. Vicini, A. Orlansky, S.L. Li, F. Zhou, J.G. Ma, et al., Pharmacokinetic model-predicted anticancer drug concentrations in human tumors, Clin. Cancer Res. 10 (2004) 8048–8058.
[127] X. Zhang, X. Zhang, L. Tao, Z. Chi, J. Xu, Y. Wei, Aggregation induced emission-based fluorescent nanoparticles: fabrication methodologies and biomedical applications, J. Mater. Chem. B 2 (2014) 4398–4414.
[128] X.R. Wang, J.M. Hu, G.Y. Zhang, S.Y. Liu, Highly selective fluorogenic multianalyte biosensors constructed via enzyme-catalyzed coupling and aggregation-induced emission, J. Am. Chem. Soc. 136 (2014) 9890–9893.
[129] Y.T. Gao, G.X. Feng, T. Jiang, C.C. Goh, L.G. Ng, B. Liu, et al., Biocompatible nanoparticles based on diketo-pyrrolo-pyrrole (DPP) with aggregation-induced red/NIR emission for in vivo two-photon fluorescence imaging, Adv. Funct. Mater. 25 (2015) 2857–2866.
[130] Y. Yuan, C.J. Zhang, S. Xu, B. Liu, A self-reporting AIE probe with a built-in singlet oxygen sensor for targeted photodynamic ablation of cancer cells, Chem. Sci. 7 (2016) 1862–1866.
[131] Y. Yuan, C.J. Zhang, M. Gao, R. Zhang, B.Z. Tang, B. Liu, Fluorescent biological probes specific light-up bioprobe with aggregation-induced emission and activatable photoactivity for the targeted and image-guided photodynamic ablation of cancer cells, Angew. Chem. Int. Ed. 54 (2015) 1780–1786.
[132] Y. Yuan, S. Xu, X. Cheng, X. Cai, B. Liu, Bioorthogonal turn-on probe based on aggregation-induced emission characteristics for cancer cell imaging and ablation, Angew. Chem. Int. Ed. 55 (2016) 6457–6461.
[133] Y. Yuan, C.J. Zhang, R.T.K. Kwok, S. Xu, R. Zhang, J. Wu, et al., Light-up probe for targeted and activatable photodynamic therapy with real-time in situ reporting of sensitizer activation and therapeutic responses, Adv. Funct. Mater. 25 (2015) 6586–6595.
[134] S.G. Reed, M.T. Orr, C.B. Fox, Key roles of adjuvants in modern vaccines, Nat. Med. 19 (2013) 1597–1608.
[135] C. Chen, Z. Song, X. Zheng, Z. He, B. Liu, X. Huang, et al., AIEgen-based theranostic system: targeted imaging of cancer cells and adjuvant amplification of antitumor efficacy of paclitaxel, Chem. Sci. 8 (2017) 2191–2198.
[136] C.Y.Y. Yu, H. Xu, S. Ji, R.T.K. Kwok, J.W.Y. Lam, X. Li, et al., Mitochondrion-anchoring photosensitizer with aggregation-induced emission characteristics synergistically boosts the radiosensitivity of cancer cells to ionizing radiation, Adv. Mater. 29 (2017) 1606167–1606176.
[137] D. Schaue, W.H. McBride, Radiotherapy and immunotherapy: a beneficial liaison? Nat. Rev. Clin. Oncol. 14 (2017) 365–379.
[138] Y. Yuan, C.J. Zhang, B. Liu, A platinum prodrug conjugated with a photosensitizer with aggregation-induced emission (AIE) characteristics for drug activation monitoring and combinatorial photodynamic–chemotherapy against cisplatin resistant cancer cells, Chem. Commun. 51 (2015) 8626–8629.
[139] C.J. Zhang, Q. Hu, G. Feng, R. Zhang, Y. Yuan, X. Lu, B. Liu, Image-guided combination chemotherapy and photodynamic therapy using a mitochondria-targeted molecular probe with aggregation-induced emission characteristics, Chem. Sci. 6 (2015) 4580–4586.
[140] K. Wang, X. Fan, L. Zhao, X. Zhang, X. Zhang, Z. Li, et al., Aggregation induced emission fluorogens based nanotheranostics for targeted and imaging-guided chemo-photothermal combination therapy, Small 12 (2016) 6568–6575.
[141] G. Jiang, J. Wang, Y. Yang, G. Zhang, Y. Liu, H. Lin, et al., Fluorescent turn-on sensing of bacterial lipopolysaccharide in artificial urine sample with sensitivity down to nanomolar by tetraphenylethylene based aggregation induced emission molecule, Biosens. Bioelectron. 85 (2016) 62–67.
[142] G. Jiang, G. Zeng, W. Zhu, Y. Li, X. Dong, G. Zhang, et al., A selective and light-up fluorescent probe for β-galactosidase activity detection and imaging in living cells based on an AIE tetraphenylethylene derivative, Chem. Commun. 53 (2017) 4505–4508.
[143] L.V. Wang, S. Hu, Photoacoustic tomography: in vivo imaging from organelles to organs, Science 335 (2012) 1458–1462.
[144] W. Zhao, Z. He, J.W.Y. Lam, Q. Peng, H. Ma, Z. Shuai, et al., Rational molecular design for achieving persistent and efficient pure organic room-temperature phosphorescence, Chem 1 (2016) 592–602.